Florian Kappe, BSc.

Coherent Control of Quantum Dots

MASTER'S THESIS

to achieve the university degree of
Diplom-Ingenieur
Master's degree programme: Technische Physik

submitted to

Graz University of Technology

Supervisor
Assoc. Prof. Dipl.-Ing. Dr. techn. Markus Aichhorn

Institute of Theoretical and Computational Physics

In collaboration with University of Innsbruck, Institute of Experimental Physics
Supervisor: Univ.-Prof. Dr. Gregor Weihs

Graz, November, 2019

Affidavit

I declare that I have authored this thesis independently, that I have not used other than the declared sources/resources, and that I have explicitly indicated all material which has been quoted either literally or by content from the sources used. The text document uploaded to TUGRAZonline is identical to the present masters thesis.

Date	Signature

Contents

1 Abstract

The scope of this thesis is to present a fibre coupled Mach-Zehndner interferometer as an electrically controlled optical pulse shaper. This setup is capable of producing arbitrary laser pulse-shapes and sequences via the precise control of a phase-shifting electro-optical modulator. The created pulses are then used to coherently excite the electronic biexciton state of a semiconductor quantum dot. Decay out of this state results in the emission of two photons, which are used to characterise successful coherent control via the observation of Rabi-oscillations. A lifetime measurement of the involved electronic states is performed to further verify the quality of the pulse generation scheme.

Although the theory of quantum mechanics has been around for more than a century, it was only in the last decades that experiments were able to observe some of its consequences such as entanglement. This is due to the high experimental requirements needed to observe quantum mechanical effects.

The recent advances in micro-fabrication, metrology, development of single-photon sources and single-photon detectors have not only paved the way towards more sophisticated experiments, but also lead to the development of devices and communication protocols that rely on the fundamentals of quantum mechanics. One of the most revolutionary implementations of quantum mechanics is the quantum computer. A quantum computer replaces the classical bit, that can either be in the state zero or one, with a quantum bit (qubit), whose state can additionally be in any superposition of zero and one. A machine that performs calculations with qubits is expected to outperform a classical computer at certain computational tasks, like factoring large numbers or searching a database [1, 2]. Several physical systems have been proposed to realise qubits, including trapped ions, superconducting circuits, nitrogen vacancy (NV) centers in diamond, electron spins in quantum dots or topological majorana particles [3–7]. All of these systems interact with their environment and subsequently suffer from decoherence, i.e. the loss of quantum information. In systems that strongly couple to the environment great efforts have to be made in order to achieve the sufficiently long coherence times needed for quantum computation, e.g. cooling the system to just a few millikelvin and/or providing ultrahigh vacuum. Another shortcoming of the above matter-qubits is that it is very hard to scale those systems up in terms of qubit number due to the need of individually addressing every qubit.

A different approach is to utilize the quantum states of photons in an all-optical implementation of quantum computation [8–11]. Advantages of such a scheme are that single photons can in principle be prepared in very large numbers given appropriate emitters like BBO crystals, single ions or quantum dots and that photons can have a virtually infinite coherence time [12]. This thesis aims to present a scheme to deterministically control a semiconductor quantum dot such that it can be used as a single-photon (photon-pair) source.

2 Theory

2.1 Quantum dots

2.1.1 Introduction

In recent years quantum dots (QDs) have emerged as an interesting platform in many scientific fields. Due to their small size of just a few nanometers, QDs show non-classical behaviour that differs significantly from bulk materials.

Self assembled gold QDs exhibit tunable plasmonic characteristics depending on their size and have become a viable tool in many applications of medicine like drug delivery or cancer treatment [13, 14].

Gated QDs formed in semiconducting materials by electrically deforming and manipulating the potential energy landscape have been proposed as candidates for matter qubits used in quantum computation [6]. Spin manipulations of single electrons loaded into QDs allow for a set of universal gates needed for state preparation [15–17]. More complex schemes for computation utilising two QDs as a single qubit and utilising singlet and triplet electron states as a computational basis have also been shown [18, 19].

Another way of forming a potential energy landscape that leads to discrete energy states is to embed a semiconducting material of appropriate size in a different semiconducting material. If the size of such a nano-structure is small in all three spatial dimensions, it is often referred to as a zero-dimensional defect or a QD. Due to the discrete states and energy levels formed in QDs (see section 2.1.2) they are excellent single photon sources that can be resonantly driven by an electromagnetic field, e.g. a laser [20]. Also, if driven into the biexciton state QDs can emit two photons that show polarisation entanglement [21]. This can be used to entangle two spatially separated quantum systems or as a source of entanglement used in quantum key distribution (QKD) [22]. If exited coherently, QDs can act as deterministic entanglement sources, which is an advantage over the commonly used spontaneous parametric down-conversion (SPDC) photon-pair sources which rely on probabilistic processes [23–25].

2.1.2 Properties of quantum dots

Embedding a semiconductor in a material with different valence and conduction band energies results in a potential energy landscape as illustrated in figure 1. When an electron or an (electron)hole is introduced into this landscape its motion will become quantized, if its de Broglie wavelength (equation (2.1)) is comparable to the dimensions of the formed potential well.

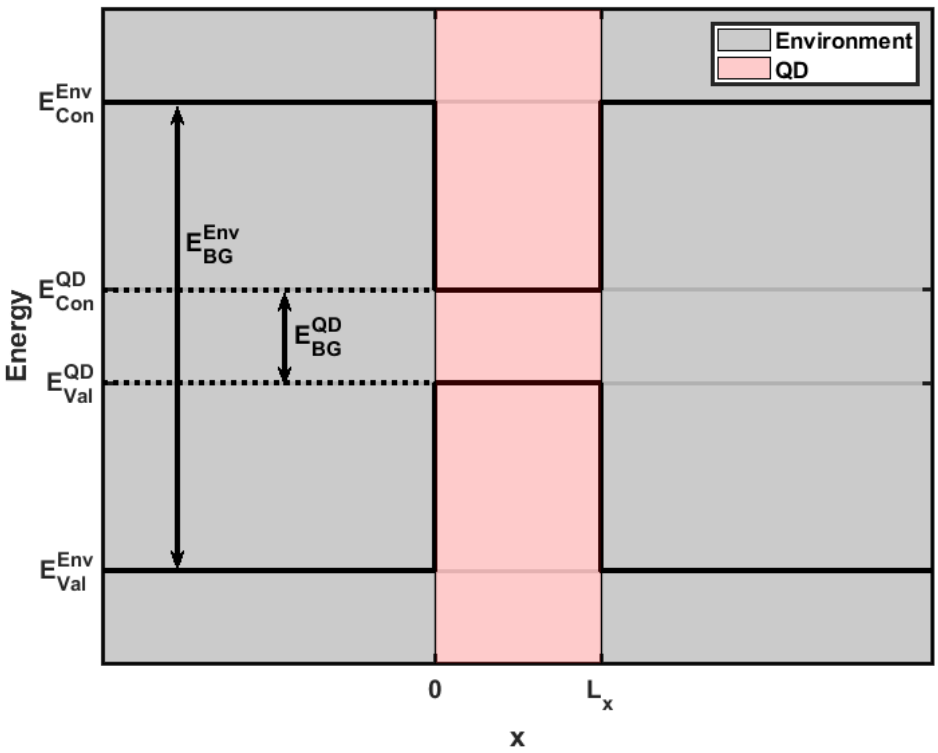

Figure 1: One-dimensional potential landscape formed by a QD and its environment. E^i_j with $i \in \{\mathrm{QD}, \mathrm{Env}\}$ and $j \in \{\mathrm{Val}, \mathrm{Con}, \mathrm{BG}\}$ correspond to the respective valence and conduction band energies of the QD and the environment and their band-gap energies. The confining potential is visible in the middle and its size in one dimension is given by $\mathrm{L_x}$. Note that both, the conduction band and valence band energies, of the QD differ from its environment, which results in quantum confinement of electrons and electron-holes alike.

$$\lambda_{DB} \approx \sqrt{\frac{2\pi\hbar^2}{m^* k_B T}} \tag{2.1}$$

An electron in a periodic crystal structure interacts with its surrounding and reacts differently to external forces than a free electron would. Examples of such external forces are electric and magnetic fields or deformation of the crystal. It is shown that if the spatial variation of such forces remains much smaller than the periodic crystal potential and the charge carriers energy is small compared to the energy gap, the periodic potential can be neglected and electrons (and holes) can be treated as free particles that have an *effective mass*, which differs from the free electron mass m_e [26]. This approximation

is referred to as the effective mass approximation which is still valid in the quantum regime. There one can use the conventional Schrödinger equation for a charged particle with its effective mass while neglecting the periodic crystal potential to describe the equations of motion of such a particle.

For an electron in a semiconductor a typical value for its effective mass is $m^* \approx 0.1 m_e$ which gives a wavelength of $\lambda_e \approx 10\,\mathrm{nm}$ at room temperature $T = 300\,\mathrm{K}$ [27].

To get an understanding of the particle's quantisation of motion and the influence of symmetry, the potential energy landscape can be approximated by a three dimensional box potential. This approximation results in quantized energy levels and is valid for electron energies much lower than the potential well's height. The calculation of eigenstates and eigenenergies of a three dimensional quantum well are found in appendix A.1.

As a result of this calculations eigenenergies in a three dimensional system like this depend on the three restricting lengths L_x, L_y, L_z as well as corresponding quantum numbers $n_x, n_y, n_z \in \mathbb{N}_{\neq 0}$.

$$E_{n_x,n_y,n_z} = \frac{\hbar^2 \pi^2}{2m^*}\left(\frac{n_x^2}{L_x^2} + \frac{n_y^2}{L_y^2} + \frac{n_z^2}{L_z^2}\right) \tag{2.2}$$

If some dimensions of the system are of the same size, e.g. $L_x = L_y \neq L_z$, there are multiple sets of quantum numbers that correspond to the same energy. This is called a degenerate system and plays an important role in entanglement generation.

2.1.3 Interaction with light

In the presence of an electromagnetic field an electron from the valence band can be excited into the conduction band via the absorption of a photon. The excited electron leaves a hole behind and the resulting electron/hole pair is called an *exciton* (X). Since the dimensions of the QD are of the same order as the de Broglie wavelength of an electron in a semiconductor their behaviour becomes quantized and only certain energies are allowed to become occupied by the exciton. A more detailed treatment of the quantum confinement effect on excitons in QDs is found in [28].

Exciting two electrons from the valence band into the lowest energy state of the confining potential results in the formation of a *biexciton* (XX). The two electrons and holes interact with each other and therefore the energy corresponding to a biexciton state is not the mere sum of two exciton energies, but differs from that by an amount called the biexciton binding energy. This shift in energy allows two-photon resonant excitation as discussed in section 2.1.4. A theoretical treatment of biexciton states in semiconductor QDs is found in [29].

If an exciton is present in the QD an additional charge in form of an extra electron or hole can also become trapped in the confining potential. Together they form negatively or positively charged excitons which are also referred to as trions (X^*). More insights into trions and excitons are found in [30].

Investigating the angular momentum of the involved particles gives insight into the radiative behaviour of the exciton/biexciton state. An electron in the conduction band has a magnetic quantum number $s_e = \frac{1}{2}$ and a spin $m_e = \pm\frac{1}{2}$. A hole has a magnetic quantum number of $s_h = \frac{3}{2}$ and can be either a so-called *light hole* with spin $m_h^l = \pm\frac{1}{2}$ or a *heavy hole* with spin $m_h^h = \pm\frac{3}{2}$. At the Γ-point these states are degenerate but split as a result of the spin-orbit interaction [26].This gives a total of eight product states $|X\rangle = |m_e\rangle_e |m_h\rangle_h$ that the exciton can be in. Introducing the angular momentum quantum number $j = s_e + s_h, s_e + s_h - 1, ..., |s_e - s_h| + 1, |s_e - s_h|$ and the total spin quantum number $m = j, j-1, ...-j+1, -j$ the possible exciton states in basis $|j, m\rangle$ can be written as:

$$\begin{aligned}
|2,+2\rangle &= \left|+\frac{1}{2}\right\rangle_e \left|+\frac{3}{2}\right\rangle_h \\
|2,+1\rangle &= \sqrt{\frac{1}{4}}\left|-\frac{1}{2}\right\rangle_e \left|+\frac{3}{2}\right\rangle_h + \sqrt{\frac{3}{4}}\left|+\frac{1}{2}\right\rangle_e \left|+\frac{1}{2}\right\rangle_h \\
|2,0\rangle &= \sqrt{\frac{1}{2}}\left|+\frac{1}{2}\right\rangle_e \left|-\frac{1}{2}\right\rangle_h + \sqrt{\frac{1}{2}}\left|-\frac{1}{2}\right\rangle_e \left|+\frac{1}{2}\right\rangle_h \\
|2,-1\rangle &= \sqrt{\frac{1}{4}}\left|+\frac{1}{2}\right\rangle_e \left|-\frac{3}{2}\right\rangle_h + \sqrt{\frac{3}{4}}\left|-\frac{1}{2}\right\rangle_e \left|-\frac{1}{2}\right\rangle_h \\
|2,-2\rangle &= \left|-\frac{1}{2}\right\rangle_e \left|-\frac{3}{2}\right\rangle_h \\
|1,+1\rangle &= \sqrt{\frac{3}{4}}\left|-\frac{1}{2}\right\rangle_e \left|+\frac{3}{2}\right\rangle_h - \sqrt{\frac{1}{4}}\left|+\frac{1}{2}\right\rangle_e \left|+\frac{1}{2}\right\rangle_h \\
|1,0\rangle &= \sqrt{\frac{1}{2}}\left|+\frac{1}{2}\right\rangle_e \left|-\frac{1}{2}\right\rangle_h - \sqrt{\frac{1}{2}}\left|-\frac{1}{2}\right\rangle_e \left|+\frac{1}{2}\right\rangle_h \\
|1,-1\rangle &= \sqrt{\frac{1}{4}}\left|-\frac{1}{2}\right\rangle_e \left|-\frac{1}{2}\right\rangle_h - \sqrt{\frac{3}{4}}\left|+\frac{1}{2}\right\rangle_e \left|-\frac{3}{2}\right\rangle_h
\end{aligned} \tag{2.3}$$

The coefficients of the above states are taken from a Clebsch-Gordan table.

Optical selection rules state that angular momentum has to be conserved during absorption/emission of a photon and only transitions in which the change in the spin-z component $\Delta m = \Delta m_e + \Delta m_h = \pm 1$ are allowed. Since the ground state of the system (QD with no confined charges, $|0\rangle = |0,0\rangle = |0\rangle_e |0\rangle_h$) has a total spin of $m = 0$ only states with $m = \pm 1$ couple to light and are referred to as *bright excitons*. States with $m = 0, \pm 2$ do not couple to light and are named *dark exciton* states respectively. A deeper treatment of the dark exciton states can be found in [31] and chapter 4 of [32].

In the case of the biexciton state ($|XX\rangle$) the electrons/holes occupy the same electronic state and the Pauli exclusion principle leads to a total spin of zero (see figure 2). A radiative transition into the unloaded (empty) ground state of the QD is therefore

possible by emitting two photons, where each emission changes the spin-z component by ± 1.

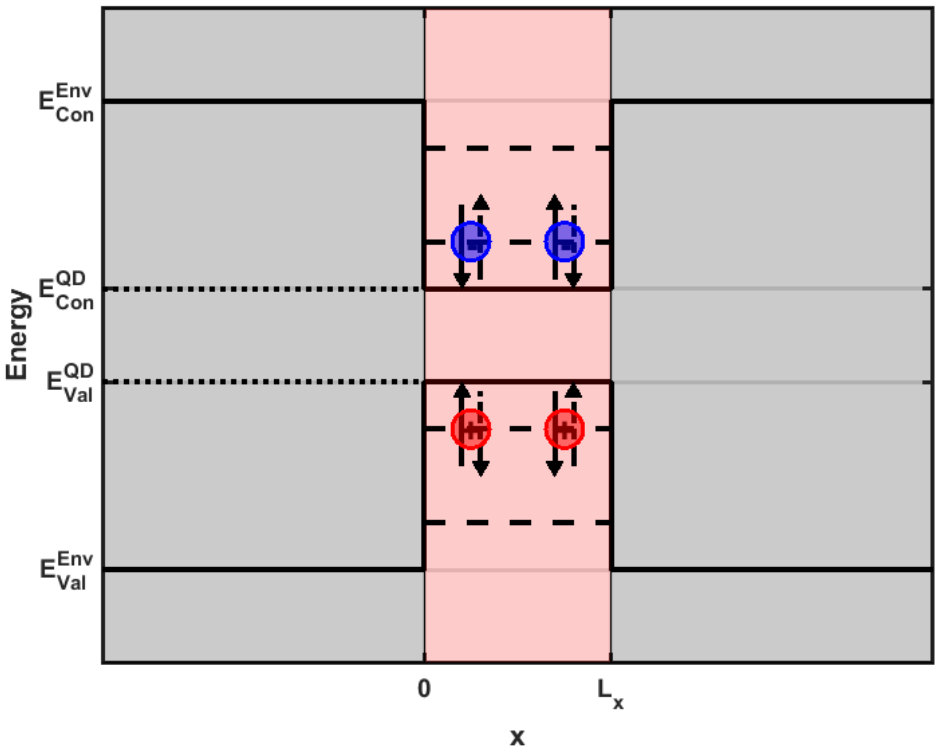

Figure 2: Spin states of the biexciton. Pauli exclusion principle forces particles occupying the same energy state to be of opposite spin and the total spin is zero. Due to the indistinguishability of the particles the actual spins of two particles occupying the same state are interchangeable (represented by the dashed arrows).

Light emission

As point sources, QDs, like atoms, usually emit light into the full solid angle and thus make collecting photons emitted by a QD embedded in a planar semiconductor sample very inefficient. This is especially true with regards to the high refractive index n_{Env} of the embedding environment and consequently total internal reflection at the interface between semiconductor and air (vacuum), as depicted in figure 3a. For a semiconductor with refractive index $n_{Env} = 3.5$, which is a typical value for InP, only $\approx 2\%$ of the emitted photons are able to leave the sample structure [33]. To overcome this issue QDs are often embedded in various cavities or photonic structures which aim to favour emission into a specific direction/emission-mode. Some of the possible structures are

shown in figure 3b.

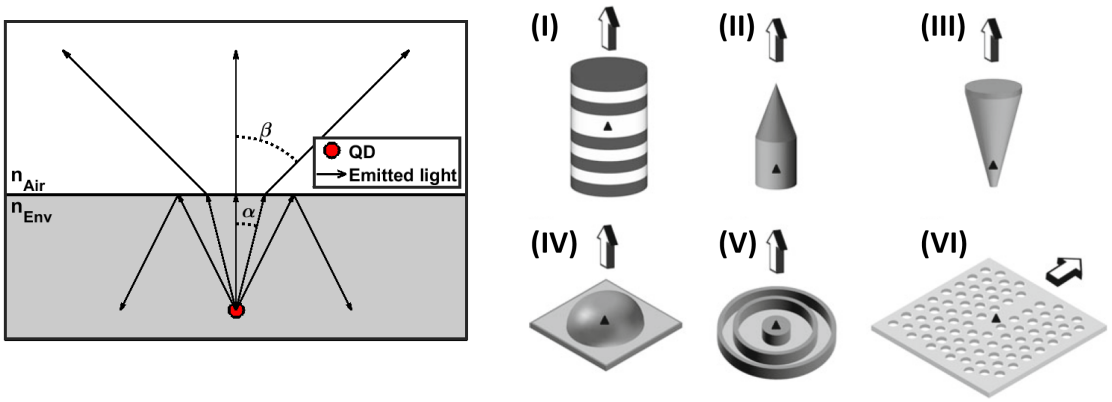

(a) Light emission of a planar sample. **(b)** Various embedding structures.

Figure 3: (a) QD embedded in a planar sample. Emitted photons get refracted according to Snell's law and are not able to leave the sample at all if the condition for total internal reflection $\alpha \geq \sin^{-1}(n_{Air}/n_{Env})$ is met. (b) Different forms of cavities or photonic structures used to favour specific emission directions indicated by an arrow. **(I)** Micropillar cavity. **(II)** Photonic nanowire. **(III)** Photonic trumpet. **(IV)** Microlens. **(V)** Bull's eye cavity. **(VI)** Photonic crystal waveguide. The QD's position is indicated by a triangle. Figure adapted from [32].

2.1.4 Excitation schemes

There are several ways to excite an exciton/biexciton state in a QD. Besides the obvious way of using resonant light three other schemes are discussed:

1. Above-band excitation.
2. Quasi-resonant excitation.
3. Two-photon resonant excitation of a biexciton.

Above-band excitation

In above band excitation a laser with photon energy larger than the band-gap energy of the surrounding material is used to create electron/hole pairs in the vicinity of the QD. Energy losses through non-radiative phonon scattering processes allow relaxation into the exciton state ($|X\rangle$) of the QD. A recombination of electron and hole then emits a photon at the characteristic exciton wavelength. This scheme is illustrated in figure 4a. An advantage of above band excitation is that it is not necessary to hit the QD directly

with the pump laser and that it can be done with a wide range of excitation wavelengths. Residual pump light can easily be removed by dichroic filters, since its wavelength is usually much shorter than the emitted exciton/biexciton photons. Although the process is probabilistic it is a reliable way of preparing an exciton state and is a valuable tool to probe the emission behaviour of QDs. On the downside, the high concentration of charge carriers in the QD's neighbourhood influences the local electric field and dephasing of the QD states is increased. Also some of the energy of the pump photon is converted into heat, which has to be taken into account in terms of stability and thermal expansion.

Quasi-resonant excitation

In quasi-resonant excitation the initial pump photon is resonant with an exited state of the QD, whose energy is higher than that of the $|X\rangle$ state. This leads to less production of charge carriers in the vicinity of the QD and a more stable state in terms of dephasing. In contrast to above-band excitation it is crucial to focus the pump light onto the QD in order to drive this transition, which makes this excitation scheme more cumbersome in terms of alignment. The used pump wavelength has to be resonant with a higher excited state of the QD which limits the usable pump sources. Although the transition into the excited state is resonant and therefore can be effected deterministically, the relaxation processes into the $|X\rangle$ state still occur randomly and limit the use of this excitation scheme as a way to implement a deterministic single photon source. The scheme is illustrated in figure 4b.

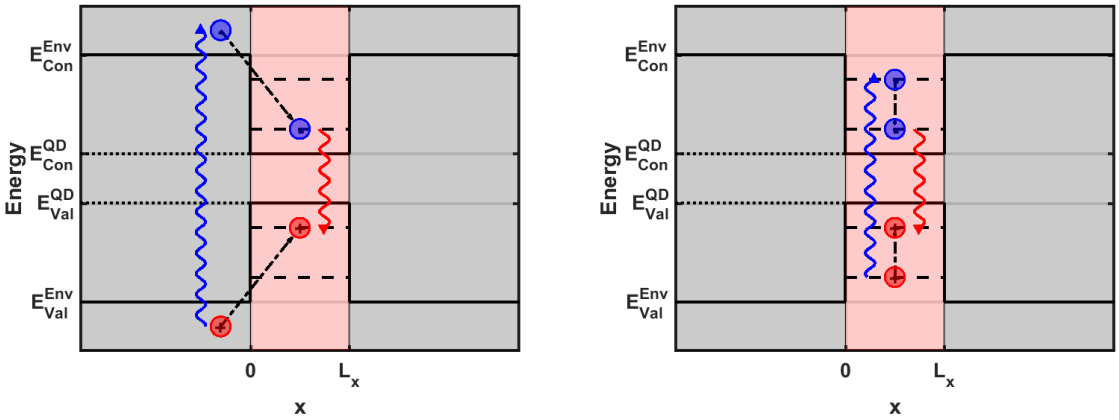

(a) Above band excitation. **(b)** Quasi resonant excitation.

Figure 4: (a) Schematics of above band excitation: A pump photon (blue) creates an electron (blue circle)/hole (red circle) pair in the vicinity of the QD which relaxes into the $|X\rangle$ state via phonon-mediated energy losses. Recombination of the charge carriers results in an emitted photon (red) at the exciton wavelength. (b) Schematics of quasi resonant excitation: A pump photon (blue) creates an electron (blue circle)/electron hole (red circle) pair in an excited state of the QD. The state relaxes into the $|X\rangle$ state and recombination of the charge carriers emits a photon at the exciton wavelength (red).

Two-photon resonant excitation of the biexciton

The $|XX\rangle$ state has a total spin of zero and optical transition rules therefore forbid excitation by a single photon. However, two-photon resonant excitation is allowed provided the polarisation state of the pump light is not purely circular. In order to drive this transition most efficiently, the pump photons have to be linearly polarised which corresponds to an equal superposition of circularly polarised photons: $|H(V)\rangle = \sqrt{\frac{1}{2}}(|\sigma_+\rangle \pm |\sigma_-\rangle)$. The two excitons present in the QD feel a binding energy which shifts the energy of the biexciton as illustrated in figure 5a. This leads to the pump photons being non-resonant with either of the transitions $|0\rangle \rightarrow |X\rangle$ or $|X\rangle \rightarrow |XX\rangle$ and coherent excitation is achieved via a virtual state. The wavelength of the pump photons is tuned to be the arithmetic mean of the emitted biexciton and exciton photons. Similar to quasi-resonant excitation this scheme suppresses the creation of free charge carriers, which favours stability in terms of dephasing and the creation of charged trions. Coherent control of the biexciton state leads to observable Rabi oscillations as discussed in section 2.4.

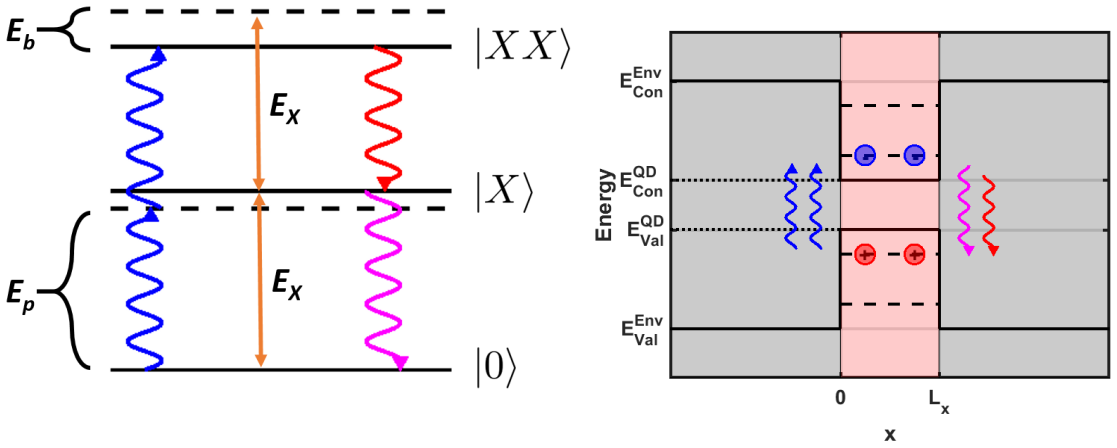

(a) Energy diagram of electronic states in a QD.

(b) Charge occupation during two-photon resonant excitation.

Figure 5: (a) Energy diagram of the biexciton excitation process: Two pump photons (blue) carry an energy of $\boldsymbol{E_p}$ and excite the biexciton state $|XX\rangle$ via a virtual energy level (dashed line in the middle). The biexciton energy if shifted by the binding energy $\boldsymbol{E_b}$ in comparison to the exciton state $|X\rangle$ with energy $\boldsymbol{E_X}$. This shift leads to the emission of a photon at a characteristic biexciton wavelength (red) accompanied by a photon at the exciton wavelength (magenta). (b) Charge occupation during two photon resonant excitation: Two pump photons (blue) simultaneously create two electron (blue circles)/hole (red circles) pairs in the QD. Recombination of the charge carriers emits two photons with different wavelengths (magenta and red).

2.2 Electro optical modulators

Some materials experience a change in their optical properties if they are subjected to an electric field. These properties include the opaqueness and the refractive index of such materials. This is a result of molecular forces that distort the orientation, position or shapes of the electronic arrangement in the used material.

In the solid state case such materials usually are of crystalline nature and have well defined lattice structures and orientations. If a direct current (DC) or low frequency alternating current (AC) electric field is applied across the material, an induced force will distort the shape of the crystal's electronic lattice depending on its orientation relative to the electric field. This change shifts the phase of passing light depending the polarisation state of the electromagnetic wave. If the interaction length is long enough, phase shifts become macroscopical and strong enough to control the phase of

the electromagnetic wave. Materials whose refractive index can be modulated via the application of electric fields have multiple uses including the following:

- Prisms that can change their refractive index are used to bend light beams to different angles and replace mechanical scanning devices.
- Phase shifters oriented correctly can act as controllable wave plates and alter the polarisation state of passing light.
- Lenses with adjustable refractive index are controllable in their focal length.
- Correctly polarised light can be phase-modulated.

An in-depth treatment of electro-optics is found in chapter 20 of [34]. Relevant aspects of electro-optical effects and phase-modulators are discussed in the following sections.

2.2.1 Electro-optical effects

Expanding the expression for the refractive index $n(E)$ for a DC or low-frequency electric field E yields the Taylor series:

$$n(E) = n_0 + k_1 E + \frac{1}{2} k_2 E^2 + \mathcal{O}(\geq 3) \tag{2.4}$$

where $n_0 = n(E = 0)$, the refractive index at zero applied field and $k_i = \frac{\mathrm{d}^i n}{\mathrm{d}E^i}$, the first and second order derivative evaluated at $E = 0$. In the literature it is conventional to rewrite the coefficients k_i as $\mathfrak{r} = -2k_1 n_0^{-3}$ and $\mathfrak{s} = -k_2 n_0^{-3}$ which are known as the electro-optical coefficients. This translates equation (2.4) into

$$n(E) = n_0 - \frac{1}{2} n_0^3 \mathfrak{r} E - \frac{1}{2} n_0^3 \mathfrak{s} E^2 + \mathcal{O}(\geq 3). \tag{2.5}$$

Materials where $\mathfrak{r} \gg \mathfrak{s}$ experience a shift in refractive index that is approximately linearly dependent on the applied electric field:

$$n(E) \approx n_0 - \frac{1}{2} n_0^3 \mathfrak{r} E. \tag{2.6}$$

This effect is called *Pockels effect* and a medium that shows such a linear behaviour is named a Pockels medium [35]. The electro optical coefficient $\mathfrak{r}$ is therefore known as the *Pockels coefficient*.

If the medium is centrosymmetric, like gases, liquids and certain crystal symmetries, equation (2.5) must be invariant under the reversal of E and $n(E) = n(-E)$. In this case $\mathfrak{r} = 0$ and equation (2.5) becomes:

$$n(E) \approx n_0 - \frac{1}{2} n_0^3 \mathfrak{s} E^2. \tag{2.7}$$

This behaviour is known as the *Kerr effect* and $\mathfrak{s}$ is named the *Kerr coefficient* [36]. The refractive index of a Kerr medium depends quadratically on the applied electric field.

2.2.2 Phase modulators

Light passing through a medium of size L and refractive index $n(E)$ accumulates a phase shift of

$$\theta = \frac{2\pi n(E)L}{\lambda_0} \tag{2.8}$$

where λ_0 is the free space wavelength. If the medium is a Pockels medium the shift in phase is approximately linearly dependent on the applied electric field and equation (2.6) and equation (2.8) yield

$$\theta \approx \theta_0 - \frac{\mathfrak{r}\pi n_0^3 LE}{\lambda_0} \tag{2.9}$$

where $\theta = 2\pi n_0 L/\lambda_0$ is the phase acquired if no electric field is applied. In practice, the electric field is usually obtained by applying a voltage V across two faces of the Pockels cell and $E = V/d$ where d is the spacing between the two contacts. This allows equation (2.9) to be rewritten in terms of the applied voltage as

$$\theta = \theta_0 - \pi\frac{V}{V_\pi} \tag{2.10}$$

where V_π is known as the half-wave voltage and is defined by

$$V_\pi = \frac{\lambda_0}{\mathfrak{r}n_0^3}\frac{d}{L}. \tag{2.11}$$

V_π corresponds to the applied voltage at which the phase shift after passing through the Pockels cell is π different to a passing without any voltage applied. Figure 6 illustrates the phase shifting behaviour of a Pockels cell. As seen in equation (2.11) V_π depends on the material the phase-modulator is made of via $\mathfrak{r}n_0^3$, the wavelength of the transmitted light λ_0 and a geometric factor d/L. Values for V_π can range between just a few volts up to several kilovolts depending on these parameters.

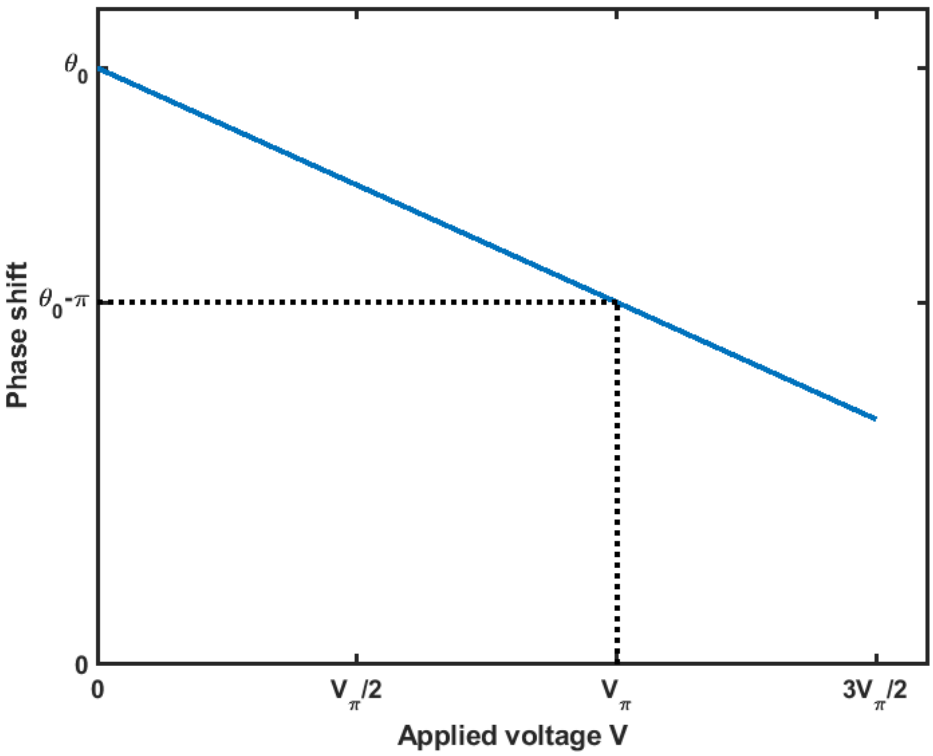

Figure 6: Phase shift of light passing through a Pockels medium. V_π is the voltage at which the phase has shifted by π compared to θ_0, the phase shift at zero applied field.

$LiNbO_3$ phase modulators

The electro-optical phase modulator (EOM) used in this thesis for pulse generation (see section 3.1) is made of lithium niobate ($LiNbO_3$). Therefore, the electro-optical behaviour of $LiNbO_3$ is discussed here in more detail.

In the case of an anisotropic material like $LiNbO_3$, the simple case described in the above section has to be expanded to account for polarisation and orientation related effects. This leads to a generalisation of equation (2.5) that reads as

$$n_{i,j}(\mathbf{E}) = n_{i,j,0} - \frac{1}{2} n_{i,j,0}^3 \sum_k \mathfrak{r}_{i,j,k} E_k - \frac{1}{2} n_{i,j,0}^3 \sum_{k,l} \mathfrak{s}_{i,j,k,l} E_k E_l + \mathcal{O}(\geq 3) \tag{2.12}$$

which is a function of the electric field vector $\mathbf{E} = (E_1, E_2, E_3)^T$. Equation (2.12) describes the polarisation dependent refractive index where $i, j, k, l \in \{1, 2, 3\}$ correspond to the three spatial dimensions. The Pockels coefficients $\mathfrak{r}_{i,j,k}$ now consist of $3^3 = 27$ elements and form a tensor of third rank. Similarly, the Kerr coefficient consists of $3^4 = 81$ elements and is a tensor of fourth rank.

Since $LiNbO_3$ is a Pockels material $\mathfrak{r}_{i,j,k} \gg \mathfrak{s}_{i,j,k,l} \ \forall \ i,j,k,l$, the last term of equation (2.12) can be neglected and only the second term contributes to a change in refractive index. Because n is symmetric, i.e. $n_{i,j} = n_{j,i}$, it has six instead of nine independent variables. It is convenient to replace the index pair (i,j) by a single index I such that the tensor $\mathfrak{r}_{I,k}$ is represented by a 6×3 matrix. The mapping from (i,j) to I is described in table 1.

Table 1: Index I corresponding to the index pair (i,j).

i,j	1	2	3
1	1	6	5
2	6	2	4
3	5	4	3

Symmetries in the crystal structure add more constraints to the Pockels coefficient tensor $\mathfrak{r}$ and fix some elements $\mathfrak{r}_{I,k}$ to be equal to zero, equal to other entries or to have the opposite sign.

$LiNbO_3$ is a member of the trigonal 3m symmetry group for which the corresponding Pockels tensor reads

$$\mathfrak{r} = \begin{pmatrix} 0 & -\mathfrak{r}_{2,2} & \mathfrak{r}_{1,3} \\ 0 & \mathfrak{r}_{2,2} & \mathfrak{r}_{1,3} \\ 0 & 0 & \mathfrak{r}_{3,3} \\ 0 & \mathfrak{r}_{5,1} & 0 \\ \mathfrak{r}_{5,1} & 0 & 0 \\ -\mathfrak{r}_{2,2} & 0 & 0 \end{pmatrix}. \tag{2.13}$$

Crystals that show this kind of symmetry are uniaxial and their polarisation dependent refractive indices have the relation $n_{11} = n_{22} = n_o, n_{33} = n_e$. If the electric field is oriented parallel to the z-axis, such that $\mathbf{E} = \mathbf{e}_z E = (0,0,E)^T$ the corresponding field dependent index ellipsoid has the form

$$(\frac{1}{n_{o0}^2} + \mathfrak{r}_{13}E)(x^2 + y^2) + (\frac{1}{n_{e0}^2} + \mathfrak{r}_{33}E)z^2 = 1 \tag{2.14}$$

The ellipsoid and the modification induced by the electric field are shown in figure 7.

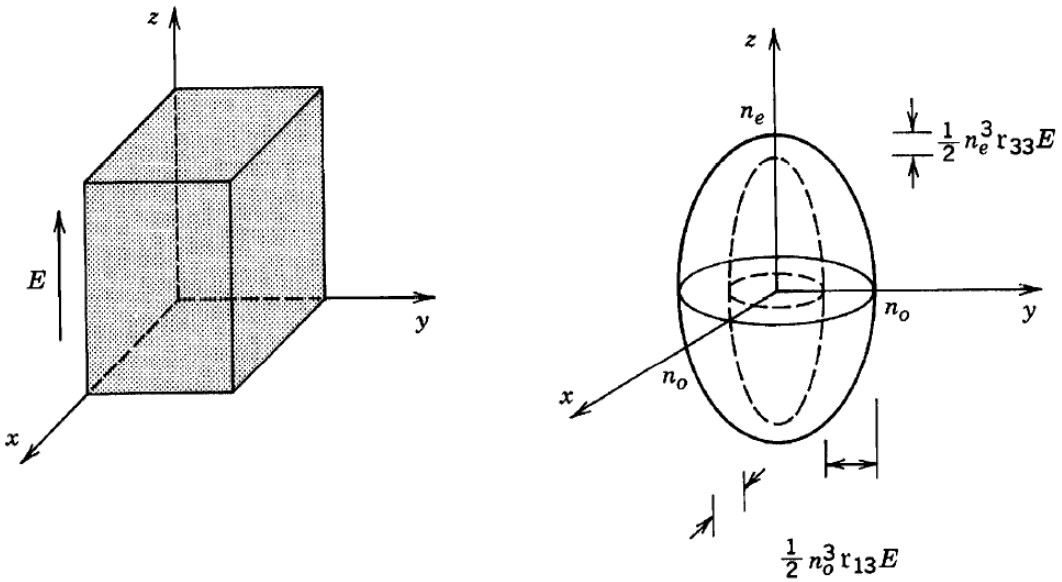

Figure 7: Left: Orientation of the electric field relative to the crystal. Right: Index ellipsoid of a trigonal 3m symmetric crystal (solid lines). Modified ellipsoid after applying a DC electric field along the z-axis (dashed lines). Figure adapted from [34].

The surface of the index ellipsoid is linked to the polarisation dependent refractive index. By intersecting a plane which passes through the origin and is perpendicular to $\mathbf{k}$, the propagation direction of the passing light, an index ellipse is constructed which describes the refractive index felt by arbitrarily polarised light. In the case of light passing through the crystal parallel to the x-y plane, e.g. $\mathbf{k} \parallel \mathbf{e}_y$, the index ellipse looks like the one depicted in figure 8 and the change in refractive index is approximated by

$$\begin{aligned} \Delta n_{11} = \Delta n_{22} = \Delta n_o \approx -\frac{n_{o0}^3 \mathfrak{r}_{13} E}{2} \\ \Delta n_{33} = \Delta n_e \approx -\frac{n_{e0}^3 \mathfrak{r}_{33} E}{2}. \end{aligned} \tag{2.15}$$

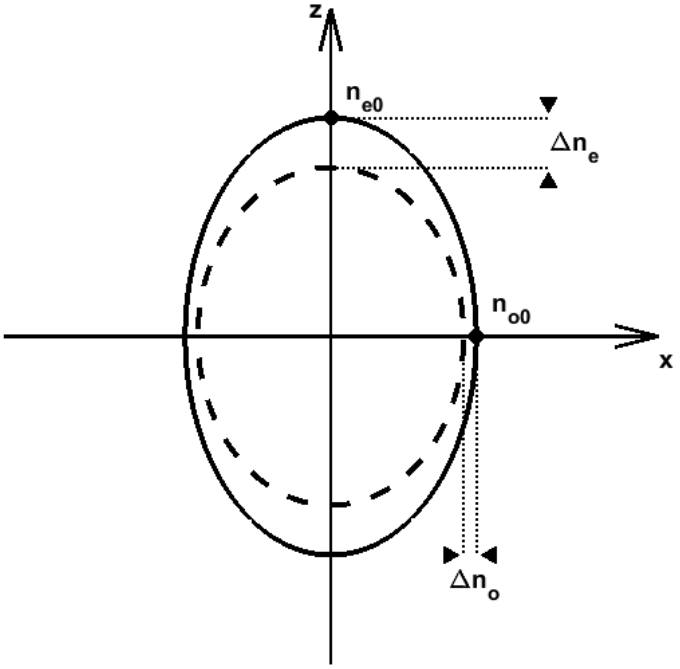

Figure 8: Index ellipse for light with $\mathbf{k} \parallel \mathbf{e}_y$ (solid line). Modified index ellipse for a static electric field $\mathbf{E} = (0, 0, E)^T$ (dashed line).

In order to use a Pockels cell made from $LiNbO_3$ as a phase modulator it is crucial to control the polarisation of the transmitted light. Since $\mathfrak{r}_{33} > \mathfrak{r}_{13}$ in $LiNbO_3$ usually the chosen polarisation is parallel to $\mathbf{e}_z$ such that it is maintained and a maximal phase shift is achieved.

Values for n_{o0}, n_{e0} and the Pockels coefficients of $LiNbO_3$ can be found in [37] and for laser light with $\lambda = 840.0\,\mathrm{nm}$ are $n_{o0} = 2.2554$ and $n_{e0} = 2.1703$, while the Pockels coefficients are approximately $\mathfrak{r}_{13} \approx 10 \times 10^{-12}\ \mathrm{m\,V^{-1}}$ and $\mathfrak{r}_{33} \approx 30 \times 10^{-12}\ \mathrm{m\,V^{-1}}$. An in-depth treatment of electro-optic modulators made from $LiNbO_3$ is presented in [38] and [39].

2.3 Signal distortion

In order to achieve fast phase modulation for pulse generation we need to apply alternating current (AC) fields to the EOM. AC transmission through electrical components suffers from frequency dependent losses and phase shifts, similar to spatial frequency losses in optical systems, which determine the resolution of an optical imaging setup. In imaging systems like microscopes, telescopes or cameras the quality of the transmit-

ted images depends on the point spread functions (PSF) and optical transfer functions (OTF) of the used optical devices like lenses, apertures or gratings. These behaviours can be described using Fourier optics. [40]

An electrical system exhibits similar behaviour and electrical components like cables, amplifiers or resistors can also be described using Fourier analysis and an impulse response function (IRF), which is the time domain equivalent to the PSF [41]. The following chapter will focus on these Fourier methods. For a more in-depth description of electrical components the reader is advised to consult [42].

2.3.1 Fourier analysis of electrical signals

The IRF is a mathematical tool to describe the output signal for a delta function input

$$\delta(t) = \begin{cases} 1 \text{ for } t=0 \\ 0 \text{ else} \end{cases}. \tag{2.16}$$

An arbitrary input signal $g(t)$ that is sent through any electrical component will have an output signal that is the convolution of the input signal with the IRF of that component, as shown in figure 9.

$$g'(t) = g(t) \circledast \mathrm{IRF}(t) = \int_{-\infty}^{+\infty} g(\tau) \cdot \mathrm{IRF}(t-\tau) d\tau \tag{2.17}$$

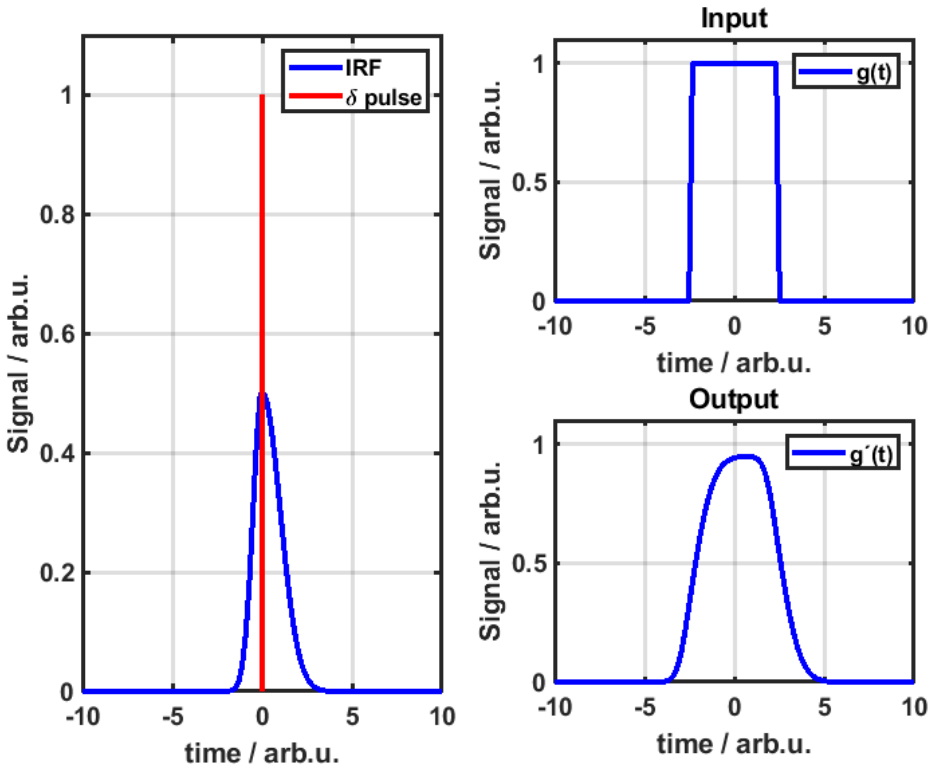

Figure 9: Effect of a IRF on a rectangular input signal. *Left*: Arbitrary IRF and delta function input. *Right*: Example of signal distortion by convolution with a IRF.

Since the convolution can be transformed into a simple multiplication via a Fourier transformation, it is convenient to work in the frequency domain,

$$\mathcal{F}\{g(t) \circledast h(t)\}(f) = \mathcal{F}\{g(t)\}(f) \cdot \mathcal{F}\{h(t)\}(f) = \tilde{G}(f) \cdot \tilde{H}(f). \tag{2.18}$$

The Fourier transform of a delta function is unity across all frequencies, therefore the Fourier transform of the IRF can be interpreted as the system's response to all frequencies, referred to as the frequency response function. For the arbitrarily chosen IRF shown in figure 9 this behaviour is illustrated in a double logarithmic *Bode-diagram* (see figure 10).

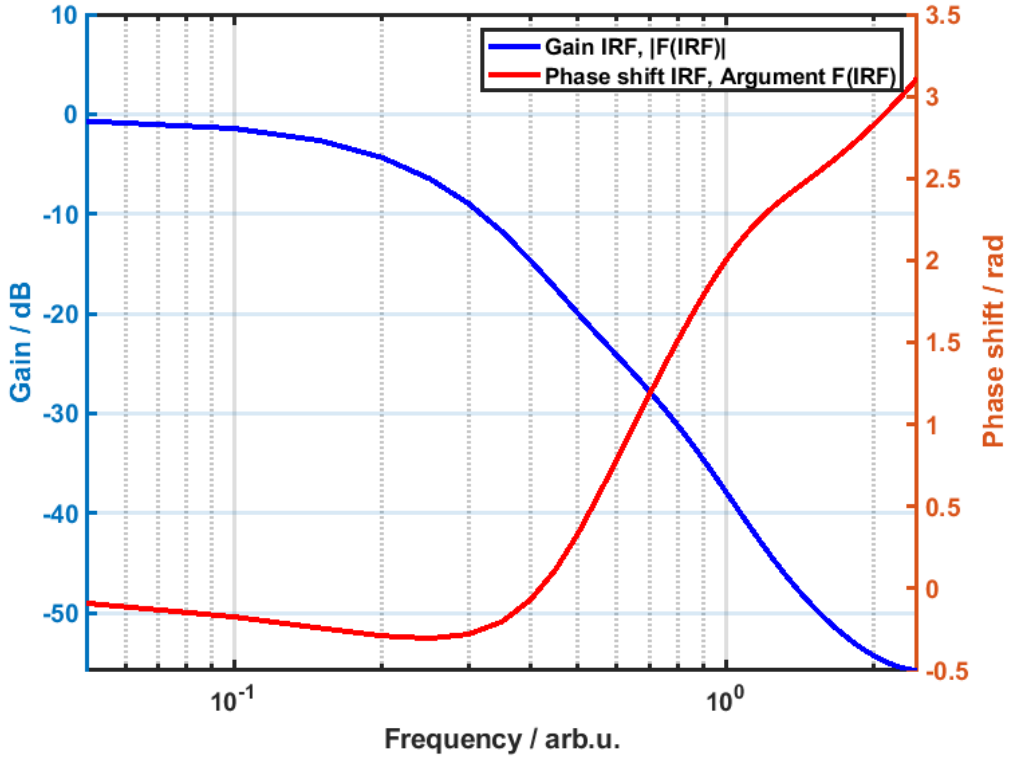

Figure 10: Bode-diagram of the arbitrary IRF displayed in figure 9. Blue: Absolute value of $\mathcal{F}\{\mathrm{IRF}(t)\}(f)$. Red: Argument of the complex value $\mathcal{F}\{\mathrm{IRF}(t)\}(f)$.

2.3.2 Correcting signal distortions with Fourier methods

As discussed in the previous section, any signal sent through an electrical component will be distorted according to equation (2.17). In order to compensate for this distortion the effect of the IRF can be reversed by adapting the input signal accordingly. Again working in the frequency domain this procedure is a simple multiplication by the inverse of the frequency response function. For a desired output signal $g'(t) = g(t)$ the input signal $\bar{g}(t)$ has to have the form

$$\bar{g}(t) = \mathcal{F}^{-1}\{\widetilde{\mathrm{IRF}}^{-1}(f) \cdot \tilde{G}(f)\}(t) \tag{2.19}$$

such that

$$g'(t) = \mathcal{F}^{-1}\{\overbrace{\widetilde{\mathrm{IRF}}(f) \cdot \widetilde{\mathrm{IRF}}^{-1}(f)}^{\mathbb{1}} \cdot \tilde{G}(f)\}(t) = g(t). \tag{2.20}$$

In order to get a well defined output signal, it is therefore necessary to know the combined frequency response function of all components between input and output. A

straight forward way to measure this is to send a delta function input through the system and record the Fourier transformation of the output.

Experimentally it is impossible to create a perfect delta function in time domain because of finite switching times. Instead this is realised by creating an input that consists of a known frequency comb (see figure 11), recording the output at these frequencies and calculating the ratio. This procedure is further referred to as a *multi-tone measurement*. Since the input is a discrete set of frequencies in the frequency domain it is not a perfect delta function input in the time domain and one has to interpolate for frequencies that are not probed.

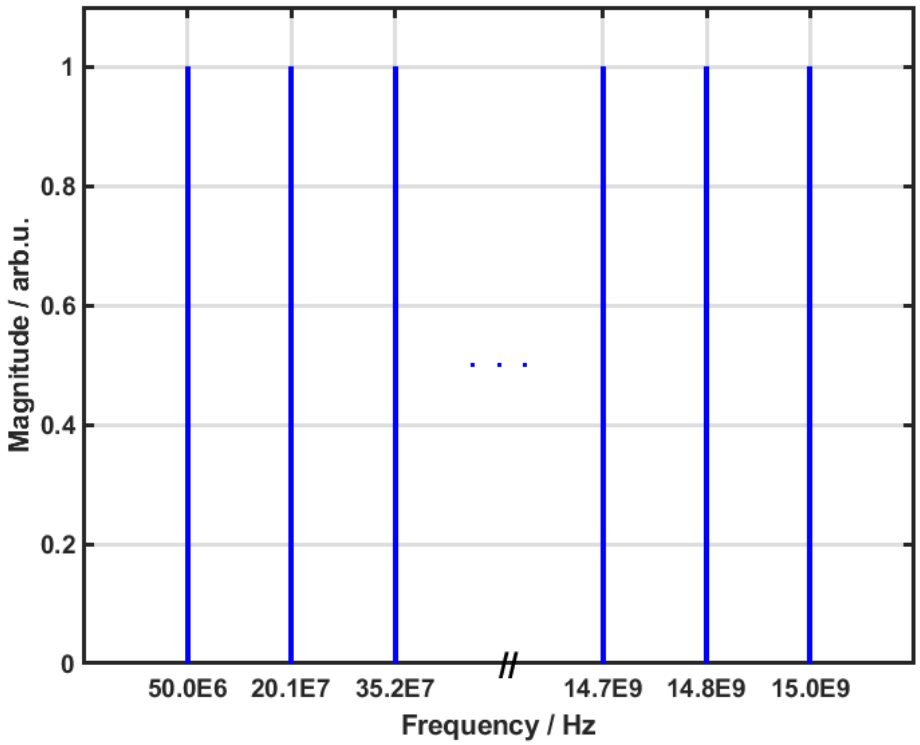

Figure 11: Frequency comb used to experimentally determine the frequency response function of the electrical system. A large number of frequency components with known positions is used in order to probe the system for frequency dependent responses.

2.4 Rabi Oscillations

Rabi oscillations are the result of a quantum mechanical two-level system under the influence of an oscillating electromagnetic field. Since this interaction is well described and understood, Rabi oscillations have emerged to become a vital tool for state prepa-

ration of physical qubits realised in trapped ions, superconducting transmon qubits or QDs embedded in solid state structures [43–45]. Because of their importance in this work, Rabi oscillations are described in more detail in the following sections, following the semi-classical approach of [46].

2.4.1 The Hamiltonian

In order to keep things clear, the case discussed here breaks down Rabi oscillations to a single electron in the Coulomb field of a non-moving nucleus. The general behaviour of this simple example translates well to more complex systems. A treatment of Rabi oscillations in two photon resonant biexciton excitation is presented in [47] and results in a qualitatively similar behaviour as the case discussed in this chapter.

The electron is influenced by a classical electromagnetic field which is completely described by a vector potential $\mathbf{A}(\mathbf{r},t)$ and a scalar potential $U(\mathbf{r},t)$. Since the atom on the other hand is described using a quantum formalism, this method is called a semi classical approach. The Hamiltonian used to describe the system is:

$$\hat{H} = \frac{1}{2m}(\hat{\mathbf{p}} - q\mathbf{A}(\hat{\mathbf{r}},t))^2 + qU(\hat{\mathbf{r}},t) \tag{2.21}$$

with $\hat{\mathbf{p}} = -i\hbar\nabla$ being the momentum operator and $\hat{\mathbf{r}}$ representing the electron position operator. Note that here $\mathbf{A}(\hat{\mathbf{r}},t)$ and $U(\hat{\mathbf{r}},t)$ contain both, the Coulomb field of the nucleus and the electromagnetic field that acts from the outside. A derivation of this Hamiltonian can be found in appendix A.2.

The electromagnetic field is related to the potentials $\mathbf{A}(\mathbf{r},t)$ and $U(\mathbf{r},t)$ via

$$\mathbf{E}(\mathbf{r},t) = -\frac{\partial \mathbf{A}(\mathbf{r},t)}{\partial t} - \boldsymbol{\nabla} U(\mathbf{r},t) \tag{2.22}$$

and

$$\mathbf{B}(\mathbf{r},t)) = \boldsymbol{\nabla} \times \mathbf{A}(\mathbf{r},t). \tag{2.23}$$

This implies an infinite amount of equivalent potential pairs $(\mathbf{A}, U)$ that describe the same electromagnetic field. These potentials can be transformed into each other via so called gauge transformations:

$$\mathbf{A}'(\mathbf{r},t) = \mathbf{A}(\mathbf{r},t) + \boldsymbol{\nabla} F(\mathbf{r},t) \tag{2.24}$$

$$U'(\mathbf{r},t) = U(\mathbf{r},t) - \frac{\partial \boldsymbol{\nabla} F(\mathbf{r},t)}{\partial t} \tag{2.25}$$

with $F(\mathbf{r},t)$ being a twice differentiable function. If the external electromagnetic field is a linearly polarised plane wave of the form:

$$\mathbf{E} = \mathbf{E}_0 \cos(\omega t - \mathbf{k}\cdot\mathbf{r}) \tag{2.26}$$

$$\mathbf{B} = \frac{\mathbf{k} \times \mathbf{E}_0}{\omega} \cos(\omega t - \mathbf{k} \cdot \mathbf{r}) \tag{2.27}$$

$$\mathbf{k} \cdot \mathbf{E_0} = 0 \tag{2.28}$$

then the so called Coulomb gauge

$$\boldsymbol{\nabla} \cdot \mathbf{A}(\mathbf{r}, t) = 0 \tag{2.29}$$

gives the corresponding potentials

$$\mathbf{A}_{Co} = -\frac{\mathbf{E}_0}{\omega} \sin(\omega t - \mathbf{k} \cdot \mathbf{r}) \tag{2.30}$$

$$U_{Co} = 0. \tag{2.31}$$

Using equation (2.24) and equation (2.25) the Coulomb gauge can be transformed into the so called Göppert-Mayer gauge via

$$F_{GM}(\mathbf{r}, t) = -(\mathbf{r} - \mathbf{r}_0) \cdot \mathbf{A}_{Co}(\mathbf{r}_0, t) \tag{2.32}$$

where $\mathbf{r}_0$ is the position of the nucleus. This transformation leads to the potentials

$$\mathbf{A}_{GM}(\mathbf{r}, t) = \mathbf{A}_{Co}(\mathbf{r}, t) - \mathbf{A}_{Co}(\mathbf{r}_0, t) \tag{2.33}$$

and

$$U_{GM}(\mathbf{r}, t) = U_{Co}(\mathbf{r}) + (\mathbf{r} - \mathbf{r}_0) \cdot \frac{\partial \mathbf{A}_{Co}(\mathbf{r}_0, t)}{\partial t}, \tag{2.34}$$

which are used to construct the Hamiltonian

$$\hat{H}_{GM} = \frac{1}{2m}(\hat{\mathbf{p}} - q\mathbf{A}_{GM}(\hat{\mathbf{r}}, t))^2 + V_{Co}(\hat{\mathbf{r}}) - \hat{\mathbf{D}} \cdot \hat{\mathbf{E}}(\mathbf{r}_0, t) \tag{2.35}$$

with V_{Co} being the regular atomic Coulomb interaction between the charge of the nucleus q_N and the electron charge q_e

$$V_{Co}(\hat{\mathbf{r}}) = \frac{q_N q_e}{4\pi\epsilon_0 \hat{\mathbf{r}}} \tag{2.36}$$

and

$$\hat{\mathbf{D}} = q(\hat{\mathbf{r}} - \mathbf{r}_0) \tag{2.37}$$

being the electric dipole operator.

Arguing that the wavelength of the electromagnetic field is much larger than the interaction volume of the system (e.g. an atom) allows the assumption of a homogeneous field and replacing $\mathbf{A}_{GM}(\hat{\mathbf{r}}, t)$ with $\mathbf{A}_{GM}(\mathbf{r}_0, t)$ via the long-wavelength approximation. Utilising equation (2.33) leaves equation (2.35) in its final form

$$\hat{H}_{GM} = \frac{\hat{\mathbf{p}}^2}{2m} + V_{Co}(\hat{\mathbf{r}}) - \hat{\mathbf{D}} \cdot \hat{\mathbf{E}}(\mathbf{r}_0, t). \tag{2.38}$$

This Hamiltonian can be split into two parts $\hat{H}_{GM} = \hat{H} = \hat{H}_0 + \hat{H}_1$ where

$$\hat{H}_0 = \frac{\hat{\mathbf{p}}^2}{2m} + V_{Co} \tag{2.39}$$

is the well known atomic Hamiltonian and

$$\hat{H}_1 = -\hat{\mathbf{D}} \cdot \mathbf{E}(\mathbf{r}_0, t) \tag{2.40}$$

represents the electric dipole or interaction Hamiltonian. $\hat{H}_1$ is linked to the description of a classical dipole moment located at $\mathbf{r}_0$ in the presence of an electromagnetic field.

A more detailed description of the Göppert-Mayer transformation and derivation of equation (2.38) can be found in [48].

2.4.2 Two level systems

Consider a system of two eigenstates $|0\rangle$ and $|1\rangle$ with energies E_0 and E_1 respectively. The difference in energy is denoted by

$$E_1 - E_0 = \hbar\omega_0. \tag{2.41}$$

In matrix representation the eigenstates of $\hat{H}_0$ translate to two two-dimensional vectors $|0\rangle = (1,0)^T$ and $|1\rangle = (0,1)^T$ and the atomic Hamiltonian (equation (2.39)) in matrix notation is of the form

$$\hat{H}_0 = \begin{pmatrix} -\frac{\hbar\omega_0}{2} & 0 \\ 0 & \frac{\hbar\omega_0}{2} \end{pmatrix} = -\frac{\hbar\omega_0}{2}\sigma_Z \tag{2.42}$$

with $\sigma_Z = \left(\begin{smallmatrix} 1 & 0 \\ 0 & -1 \end{smallmatrix}\right)$ being the third Pauli matrix. The interaction Hamiltonian (equation (2.40)) describes the coupling of states $|0\rangle$ and $|1\rangle$ and, represented by the matrix W, can be written as

$$W_{00} = W_{11} = -\langle 0|\hat{\mathbf{D}} \cdot \mathbf{E}(\mathbf{r}_0)|0\rangle = -\langle 1|\hat{\mathbf{D}} \cdot \mathbf{E}(\mathbf{r}_0)|1\rangle = 0 \tag{2.43}$$

and

$$W_{10} = W_{01} = -\langle 1|\hat{\mathbf{D}} \cdot \mathbf{E}(\mathbf{r}_0)|0\rangle = -\langle 0|\hat{\mathbf{D}} \cdot \mathbf{E}(\mathbf{r}_0)|1\rangle = \hbar\Omega_0. \tag{2.44}$$

Here a Rabi frequency Ω_0 has been introduced that determines the strength of the coupling between the two states. For a periodic electromagnetic field as in equation (2.26) the full Hamiltonian of this two level system now reads as

$$\hat{H} = \hat{H}_0 + \hat{H}_1 = \hbar(-\frac{\omega_0}{2}\sigma_Z + \Omega_0 \cos(\omega t)\sigma_X) = \hbar \begin{pmatrix} -\frac{\omega_0}{2} & \Omega_0 \cos(\omega t) \\ \Omega_0 \cos(\omega t) & \frac{\omega_0}{2} \end{pmatrix} \tag{2.45}$$

with ω being the frequency of the electromagnetic field and $\sigma_X = \left(\begin{smallmatrix} 0 & 1 \\ 1 & 0 \end{smallmatrix}\right)$ representing the first Pauli matrix. Applying a rotating wave approximation and solving for the time dependent transition probability of a system that was prepared in the initial state $|\Psi(t_0)\rangle = |0\rangle$ yields

$$P_{0\to1}(t_0, t) = \frac{\Omega_0^2}{\Omega^2} \sin^2\left(\frac{\Omega \cdot (t - t_0)}{2}\right) \tag{2.46}$$

where $\Omega^2 = \Omega_0^2 + \Delta^2$ with $\Delta = \omega_0 - \omega$ being the detuning of the electromagnetic and atomic transition frequencies. A detailed calculation of the transition probability (equation (2.46)) is shown in appendix A.3.

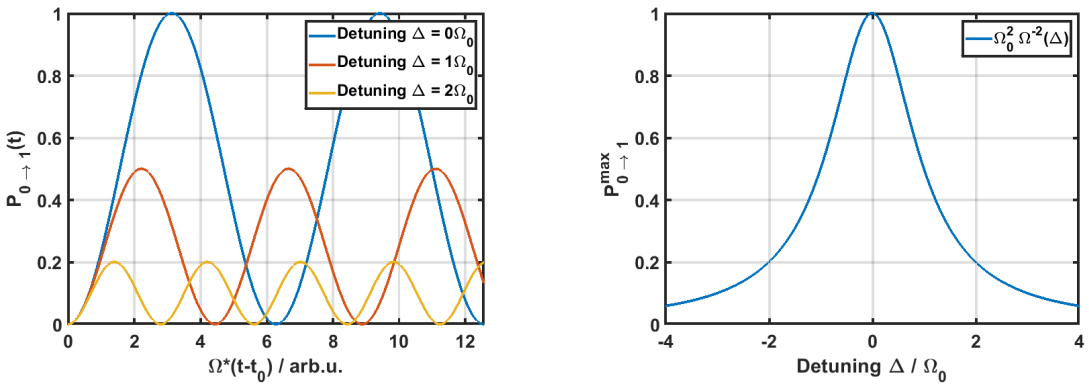

(a) Rabi oscillations for different amounts of detuning Δ.

(b) $P_{0\to1}^{max}$ for different amounts of detuning Δ.

Figure 12: Visualisation of equation (2.46). (a) Oscillating behaviour of the transition probability for different amounts of detuning. Higher detuning leads to a higher generalized Rabi frequency but lowers the maximum transition probability. (b) Maximum transition probability as a function of the detuning Δ. For $\Delta = 0$ a maximum transition probability of unity is reached.

The important properties of equation (2.46) are visualized in figure 12. On the right hand side the maximum transition probability for continuous variation of Δ shows a Lorentzian shape and a maximum of $P_{0\to1}^{max} = 1$ is found at zero detuning. Figure 12a shows the behaviour of $P_{0\to1}$ for increasing $\Omega \cdot (t - t_0)$ for different values of detuning. This results in a scheme for deterministically preparing a quantum system if the initial state is known.

Usually the ground state $|0\rangle$ of the quantum system can reliably be prepared by removing enough energy from the system, typically by cooling. Exposing the system to an electromagnetic field with zero detuning lets the system evolve according to equation (2.46) and if $\Omega(t - t_0) = (2n + 1)\pi$ with $n \in \mathbb{N}_0$ is deterministically prepared into $|1\rangle$. This procedure of turning a resonant AC field on for a defined amount of time and with an appropriate strength is know as a π-pulse. If the transition back into $|0\rangle$ is radiant and emits a photon, the system can be used as a deterministic single photon source [20]. By applying a pulse with $\Omega(t - t_0) = \frac{(2n+1)}{2}\pi$ the state can be rotated into the superposition state $|+\rangle = \frac{1}{\sqrt{2}}(|0\rangle + |1\rangle)$ which is known as a $\frac{\pi}{2}$-pulse. The effect of these two pulses on the ground state are shown in figure 13.

(a) Induced rotation on the Bloch-sphere for a π-pulse.

(b) Induced rotation on the Bloch-sphere for a $\frac{\pi}{2}$-pulse.

Figure 13: Actions on the Bloch-sphere. Blue arrows represent the initial states and red arrows correspond to the final states. Solid red lines indicate the rotations performed during the interaction time.

2.4.3 Decoherence in quantum dots

In a system that consists of an embedded semiconductor QD multiple decoherence mechanisms like a phonon-induced shift in the Rabi frequency or a drive dependent damping exist [49–51]. In the case of phonon-damped Rabi oscillations multiple theoretical models have been developed that describe the dynamics of a two-level system in contact with a bosonic environment. The usual goal of these models is to derive a master equation that relates the evolution of density-matrix elements to environmental parameters. Practical master equations always involve some approximations and for a QD system are commonly derived in two separate regimes. The weak-coupling approach relies on weak exciton-phonon coupling [52–54], while stronger coupling is described via a polaron transform method and further discussed in [55–57]. A general approach that aims to

unify those regimes via a variational master equation approach is presented in [58].

All of the above methods start by modifying the undisturbed two-level Hamiltonian of equation (2.45) by adding additional phonon terms:

$$\hat{H} = \omega_0 \left|1\right\rangle\!\left\langle 1\right| + \Omega_0 \cos(\omega t)\sigma_X + \sum_{\mathbf{k}} \omega_{\mathbf{k}} b_{\mathbf{k}}^\dagger b_{\mathbf{k}} + \sum_{\mathbf{k}} (g_{\mathbf{k}} b_{\mathbf{k}}^\dagger + g_{\mathbf{k}}^* b_{\mathbf{k}}) \left|1\right\rangle\!\left\langle 1\right| . \tag{2.47}$$

The first two terms of the Hamiltonian describe the regular undisturbed system and follow the same nomenclature as equation (2.45) (using Bohr units: $\hbar = 1$). The last two terms introduce a phonon bath, represented by an infinite number of harmonic oscillators with frequencies $\omega_{\mathbf{k}}$ and creation (annihilation) operators $b_{\mathbf{k}}$ ($b_{\mathbf{k}}^\dagger$). The exciton-phonon coupling strength is denoted with $g_{\mathbf{k}}$. Depending on the used methods and regime, several transformations and approximations are performed on equation (2.47), which are beyond the scope of this thesis.

In [58] a comparison of weak-coupling theory, polaron theory, the variational master equation approach and a numerical simulation of density-matrix dynamics via the quasi-adiabatic propagator path integral (QUAPI) method is shown. These simulations are displayed in figure 14 and are in qualitative agreement with the experimental data presented in section 3.2.1. All of the displayed theories predict that for longer interaction time the excited state population converges towards 0.5 and that the maximum achievable population probability is below unity.

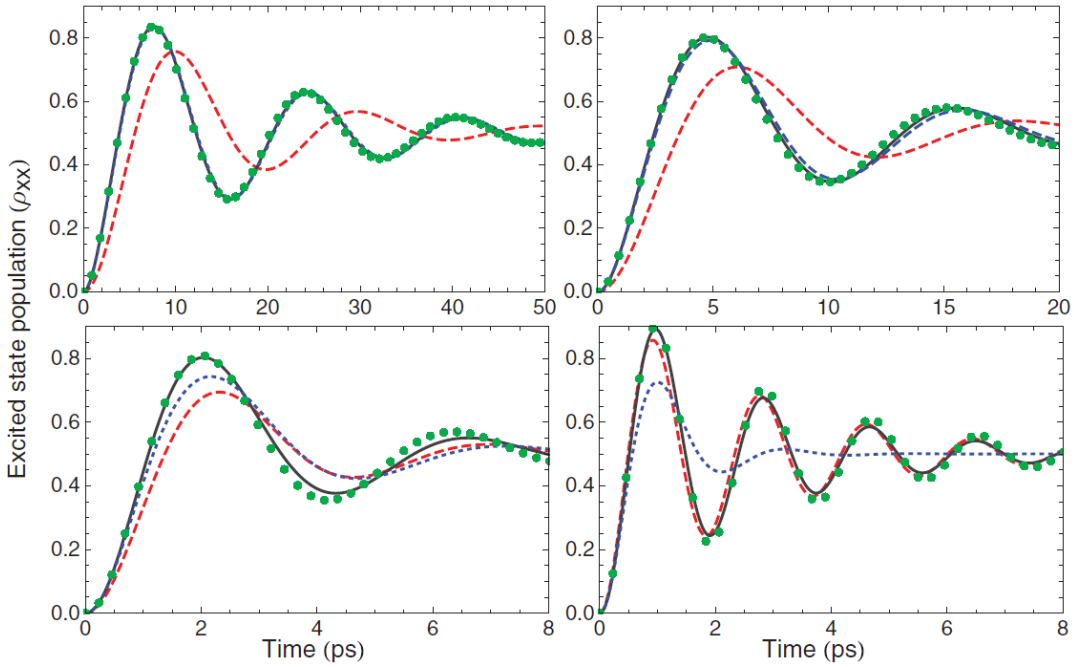

Figure 14: Exciton population dynamics calculated from the variational master equation (gray solid curves), weak-coupling theory (red dashed curves), polaron theory (blue dotted curves), and the QUAPI (green points) depending on the interaction time of a resonant electric field at a temperature of 50 K. *Top left*: $\Omega_0 = \pi/6\,\mathrm{ps}^{-1}$. *Top right*: $\Omega_0 = \pi/4\,\mathrm{ps}^{-1}$. *Bottom left*: $\Omega_0 = \pi/2\,\mathrm{ps}^{-1}$. *Bottom right*: $\Omega_0 = \pi\,\mathrm{ps}^{-1}$. Figure taken from [58].

2.5 Life time measurements

Exciting a QD and performing time-resolved photoluminescence spectroscopy gives insight into the lifetimes of the excited states of the QD [59, 60]. For resonant excitation of the biexciton state, there are two emitted photons for each excitation at different wavelengths (see section 2.1.4). This purely resonant case can be modelled via a two level system where one level feeds into the other as depicted by the two rate equations:

$$\begin{aligned} \frac{\mathrm{d}N_{\mathrm{XX}}}{\mathrm{d}t} &= -\Gamma_{\mathrm{XX}} N_{\mathrm{XX}} \\ \frac{\mathrm{d}N_{\mathrm{X}}}{\mathrm{d}t} &= -\Gamma_{\mathrm{X}} N_{\mathrm{X}} + \Gamma_{\mathrm{XX}} N_{\mathrm{XX}}. \end{aligned} \tag{2.48}$$

N_{XX} and N_{X} are the respective numbers of particles in the biexciton and exciton state and are analogous to the probability of collecting a photon emitted from the corresponding energy states. Γ_{XX} and Γ_{X} represent the rates at which particles decay out of that state. The lifetimes of the states are given by the inverse of the decay rates:

$$\begin{aligned} \tau_{\mathrm{XX}} &= \frac{1}{\Gamma_{\mathrm{XX}}} \\ \tau_{\mathrm{X}} &= \frac{1}{\Gamma_{\mathrm{X}}}. \end{aligned} \tag{2.49}$$

Solving the coupled ordinary differential equations (ODEs, equation (2.48)) is shown in appendix A.4 and yields the time dependent expressions for N_{XX} and N_{X}:

$$\begin{aligned} N_{\mathrm{XX}} &= N_0 e^{-\Gamma_{\mathrm{XX}} t} \\ N_{\mathrm{X}} &= N_0 \frac{\Gamma_{\mathrm{XX}}}{\Gamma_{\mathrm{XX}} - \Gamma_{\mathrm{X}}} (e^{-\Gamma_X t} - e^{-\Gamma_{\mathrm{XX}} t}). \end{aligned} \tag{2.50}$$

N_0 represents the total number of particles excited into the biexciton state and it is assumed that all particles start off in the biexciton state. The behaviour of equation (2.50) is illustrated in figure 15 for $\Gamma_{\mathrm{XX}} = 2\Gamma_{\mathrm{X}}$.

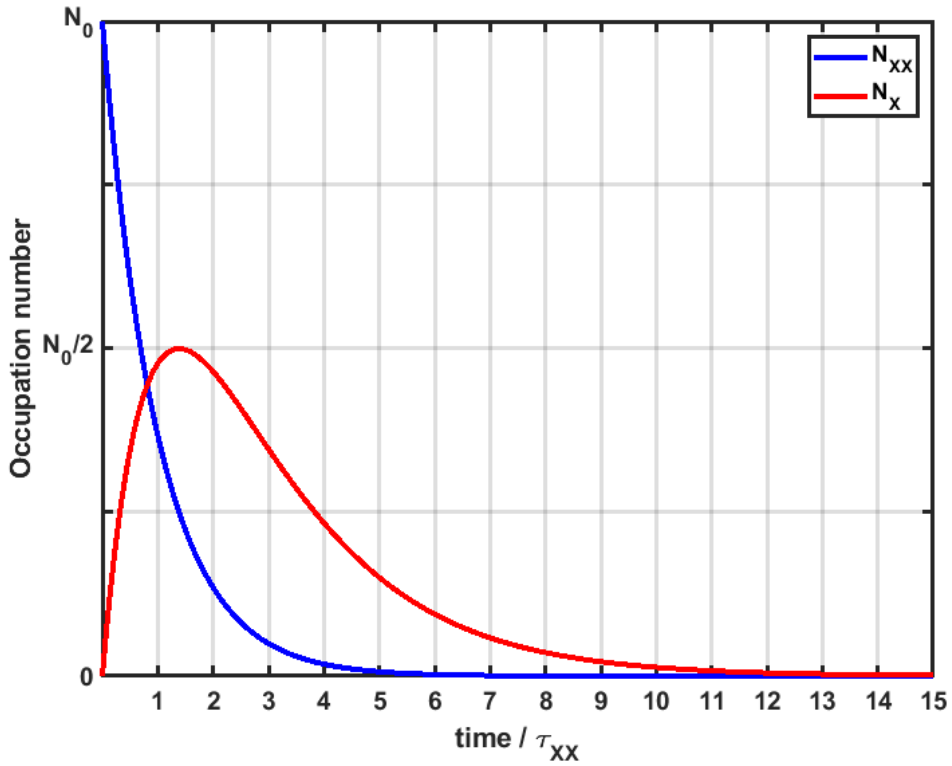

Figure 15: State occupation of a coupled two level system where the XX state feeds into the X state as described by equation (2.50). Here $\tau_{\mathrm{X}} = 2\tau_{\mathrm{XX}}$ and time is scaled in therms of τ_{XX}.

3 Experiment

In the last decades several physical systems have been proposed to realise qubits for quantum information technologies. Those systems include trapped ions, superconducting circuits, nitrogen vacancy (NV) centres in diamond, electron spins in QDs, topological majorana particles and single photons. [3–8]. In 2000 DiVincenzo formulated five criteria that have to be met for efficient quantum computation in any platform. These criteria are stated in [61] and read as follows:

1. A scalable physical system with well characterised qubits.
2. The ability to initialize the state of the qubits to a simple fiducial state.
3. Long relevant decoherence times, much longer than the gate operation time.
4. A "universal" set of quantum gates.
5. A qubit-specific measurement capability.

Two additional criteria have to be fulfilled for quantum communication:

6. The ability to interconvert stationary and flying qubits.
7. The ability to faithfully transmit flying qubits between specified locations.

A universal set of quantum gates requires the ability to perform state rotations around at least two different axes of the Bloch-sphere plus an implementation of at least one entanglement creating gate (e.g. a C-Not operation or a C-Phase gate). The term flying qubit refers to an implementation of physically sending a qubit from one party to another. QDs have emerged as a promising platform for both, the use as a solidstate qubit via electron spin manipulation and as a source for quantum light, which is the obvious choice for a flying qubit.

In the case of electron spin qubits the computational basis consists of the two spin states $|0\rangle = |\uparrow\rangle$ and $|1\rangle = |\downarrow\rangle$ which are energetically split by applying a magnetic field, known as the Zeemann-effect. Exposing the resulting two-level system to a resonant AC field in the microwave regime results in Rabi oscillations, which corresponds to a controlled state rotation around the y-axis, if the exposure time is controlled correctly (see section 2.4.2). Rotations around the z-axis are achieved by simply letting the system evolve according to its undisturbed Hamiltonian (equation (2.42)) which results in the unitary transformation $\hat{U} = e^{-i\frac{\omega_0}{2}\sigma_z t}$. To implement a universal set of quantum gates, entanglement between two QDs has to be generated. This can be achieved by electrically controlling the exchange interaction of two neighbouring QDs via a gated potential barrier [15].

If the QD is a single photon (photon-pair) source, the two-level system of interest consists of the empty ground-state $|0\rangle$ and a radiant state, e.g. the exciton (biexciton)

state $|X\rangle$ ($|XX\rangle$) (see section 2.1.3). This shifts the frequency of the AC field necessary for Rabi oscillations from the microwave regime into the optical regime. State rotations around the y-axis in this regime are achieved by the use of resonant laser pulses where the amount of rotation depends on the length and field intensity of the pulses.

Recent works on QDs show that exotic states of light, like hyper-entangled photon-pairs or photon cluster-states can be produced via precise control of excitation pulses [62, 63]. This thesis now presents a way of creating arbitrary laser pulse shapes and sequences via the use of a phase-shifting electro-optical modulator (EOM) and tests for coherent control of a QD embedded in a nanowire.

Continuous wave (CW) laser light is tuned to resonantly excite the $|XX\rangle$ state of a QD via a two photon process as discussed in section 2.1.4. A pulse generation setup, implemented and characterised as part of this thesis, is used to shape the laser light into arbitrary pulse shapes to control the energy deposition time during one iteration of the performed experiments. The experimental setup is thematically and spatially split into two parts:

1. Pulse generation setup
2. Quantum dot setup

To send pulses from the pulse generation setup towards the QD setup a polarisation maintaining single mode fibre (PM fibre) is used.

Section 3.1 discusses the working principle of the pulse generation setup and ends with a comparison of created pulse shapes and expected ones. Section 3.2 focusses on the interaction of the QD sample with the pump pulses. Coherent excitation is probed via the observation of Rabi oscillations (see section 2.4) and an extraction of different lifetimes of the excited states of the QD sample is done by time resolved photoluminescence spectroscopy.

3.1 Pulse generation setup

Coherent control of radiative/bright states in a QD is achieved by applying a laser pulse to the system. A straight forward choice would be to use a pulsed laser to excite the system, which has the advantage that pulsed lasers are readily available at different wavelengths and high quality. However, since the repetition rate of such a laser is fixed, creating more complex pulse sequences (e.g. spin-echo sequences) requires additional optical components to control spacing and intensity of individual pulses [64]. An additional limitation of pulsed lasers is that it is not possible to create pulse sequences with arbitrary pulse shapes.

In this work a pulse generation setup consisting of a fibre-coupled Mach-Zehnder interferometer (MZI) in combination with a phase-shifting EOM is used (see optical setup in figure 16). A first beam splitter divides a CW laser beam into the two arms

of the MZI that are recombined at a second beam splitter. Interference at the second beam splitter determines the ratio of the two output ports of the MZI depending on the relative phase between the two arms. A detailed mathematical treatment of a MZI is shown in equation (3.2). This setup can create arbitrary pulse sequences and pulse shapes by controlling the time dependent phase shift induced by the EOM.

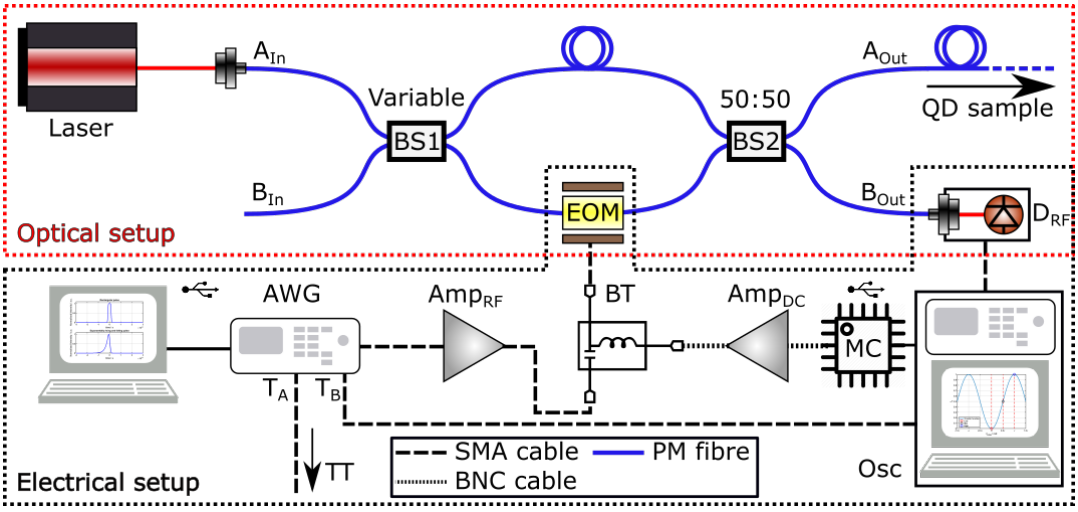

Figure 16: Pulse generation setup. *Optical setup*: Fibre coupled MZI. A CW laser source (Laser) is coupled into one input port (A_{In}) of a variable beam splitter (BS1), which splitting ratio can be tuned via the use of a micrometer-screw. One output of BS1 is sent through a phase shifting electro-optical modulator (EOM) before being recombined with the second output at a fixed beam splitter with splitting ratio 50:50 (BS2). The final output ports of the MZI are then fibre coupled towards the QD sample (A_{Out}) and onto a fast photo diode (D_{RF}) via B_{Out}. D_{RF} monitors the state of the MZI and is connected to the electrical part of the setup. *Electrical setup*: The signal of D_{RF} is processed on an oscilloscope (Osc) and a custom written algorithm determines the current operating point of the MZI. A micro-controller (MC) in combination with a home-made amplifier (AMP_{DC}) feeds DC voltage into a bias tee (BT) to stabilize the operating point of the MZI. Electrical pulse shapes are generated via an arbitrary waveform generator (AWG) and amplified by a high frequency amplifier (AMP_{RF}) before being sent through the BT into the EOM. The AWG provides two different trigger signals (T_A and T_B). T_A is sent towards a time tagger (TT) and triggers the arrival of excitation pulses while T_B is used by the Osc during drift stabilisation. More component details are found in table 2.

Table 2: Components of the pulse generation setup depicted in figure 16.

Component	Abbreviation	Manufacturer	Model
Laser source	Laser	M Squared	SolsTiS
Beam splitter	BS1	Evanescent Optics	905P
Phase shifting EOM	EOM	IXblue	NIR-MPX800-LN-20
Beam splitter	BS2	Thorlabs	PN850R5A2
Photo diode	D_{RF}	Thorlabs	DXM30AF
Oscilloscope	Osc	Tektronix	DPO71604C
Micro-controller	MC	National Instruments	NI6009
Amplifier	AMP_{DC}	Home made	-
Bias tee	BT	Mini-Circuits	ZX85-12G-S+
Arbitrary waveform generator	AWG	Keysight	M8195A 65[GSa/s]
Amplifier	AMP_{RF}	IXblue	DR-AN-20-HO
Time tagger	Tt	PicoQuant	HydraHarp 400

3.1.1 Optical setup

The optical setup of the experiment consists of a fibre-coupled MZI which consists of one variable beam splitter (BS1), one fixed beam splitter (BS2) and a phase shifting electro-optical modulator (EOM) in one of the arms. The splitting ratio of BS1 can be adjusted via a micrometer-screw, which is needed to compensate for the different losses in the two arms of the MZI. All fibres used are PM fibres with angled physical contact (APC) mating, which reduces losses induced by back-reflection. A mathematical treatment of a MZI in matrix representation is achieved by sandwiching a path dependent transmission matrix ($T_{1/2}$) in between two beam splitter matrices ($BS_{1(2)}$):

$$\mathbf{I}_{\mathrm{Out}} = \mathrm{BS}_2 \cdot \mathrm{T}_{1/2} \cdot \mathrm{BS}_1 \cdot \mathbf{I}_{\mathrm{In}}. \tag{3.1}$$

The power in both output ports ($\mathbf{I}_{\mathrm{Out}}$) depends on the splitting ratios of $BS_{1(2)}$, the losses in both arms and the relative phase difference contained in the transmission matrix $T_{1/2}$. For the setup described above this relation can be written as

$$\begin{pmatrix} A_{\mathrm{Out}} \\ B_{\mathrm{Out}} \end{pmatrix} = \begin{pmatrix} \cos(\phi_{\mathrm{fix}}) & i\sin(\phi_{\mathrm{fix}}) \\ i\sin(\phi_{\mathrm{fix}}) & \cos(\phi_{\mathrm{fix}}) \end{pmatrix} \begin{pmatrix} T_1 e^{i\theta_1} & 0 \\ 0 & T_2 e^{i\theta_2} \end{pmatrix} \begin{pmatrix} \cos(\phi_{\mathrm{var}}) & i\sin(\phi_{\mathrm{var}}) \\ i\sin(\phi_{\mathrm{var}}) & \cos(\phi_{\mathrm{var}}) \end{pmatrix} \begin{pmatrix} A_{\mathrm{In}} \\ B_{\mathrm{In}} \end{pmatrix} \tag{3.2}$$

where $\phi_{\mathrm{fix(var)}}$ determines the splitting ratio of the fixed (variable) beam splitter, $T_{1(2)}$ represents the transmission coefficients of the components in between BS1 and BS2 and $\theta_{1(2)}$ describes the phases introduced in the two arms. Since the output intensity $I_{\mathrm{A(B)}} = \|A(B)_{\mathrm{Out}}\|^2$ (up to a constant factor) only depends on $T_{1/2}$ via the relative phase

difference $\theta_1 - \theta_2$ and the transmission ratio $\frac{T_1}{T_2}$, pulling out and dropping a common factor of $T_2 e^{i\theta_2}$ allows equation (3.2) to be rewritten as

$$\begin{pmatrix} A_{\mathrm{Out}} \\ B_{\mathrm{Out}} \end{pmatrix} = \begin{pmatrix} \cos(\phi_{\mathrm{fix}}) & i\sin(\phi_{\mathrm{fix}}) \\ i\sin(\phi_{\mathrm{fix}}) & \cos(\phi_{\mathrm{fix}}) \end{pmatrix} \begin{pmatrix} \frac{T_1}{T_2} e^{i(\theta_1-\theta_2)} & 0 \\ 0 & 1 \end{pmatrix} \begin{pmatrix} \cos(\phi_{\mathrm{var}}) & i\sin(\phi_{\mathrm{var}}) \\ i\sin(\phi_{\mathrm{var}}) & \cos(\phi_{\mathrm{var}}) \end{pmatrix} \begin{pmatrix} A_{\mathrm{In}} \\ B_{\mathrm{In}} \end{pmatrix}. \tag{3.3}$$

Introducing θ_{EOM} and θ_{DC} as the AC and DC phase shifts delivered by the EOM (via AWG and BT) such that

$$\theta_{\mathrm{EOM}} + \theta_{\mathrm{DC}} = \theta_1 - \theta_2 \tag{3.4}$$

gives two desired operation points of the MZI. Maximum contrast in the optical pulse is reached for $\theta_{\mathrm{EOM}} \in \{0, \pi\}$ and stabilizing $\theta_{\mathrm{DC}} = 0$ results in the desired pulse shape in one of the output ports and an inverse shape in the other. Changing to an operating point where $\theta_{\mathrm{DC}} = \pi$ switches the two output signals.

In order to achieve the maximum visibility for the pulse sequence sent towards the QD sample, it is necessary to adjust BS1 in such a way that it compensates for the difference in T_1 and T_2. A calculation of I_{A} and I_{B} for $\theta_{\mathrm{EOM}} \in \{0, \pi\}$ dependent on ϕ_{var} is shown in figure 17. The visibility and the contrast of the interference are defined by

$$V_{\mathrm{i}} = \frac{I_{\mathrm{i}}^{\max} - I_{\mathrm{i}}^{\min}}{I_{\mathrm{i}}^{\max} + I_{\mathrm{i}}^{\min}} \tag{3.5}$$

and

$$C_{\mathrm{i}} = \frac{I_{\mathrm{i}}^{\max} - I_{\mathrm{i}}^{\min}}{I_{\mathrm{i}}^{\min}} \tag{3.6}$$

where $\mathrm{i} \in \{\mathrm{A}, \mathrm{B}\}$.

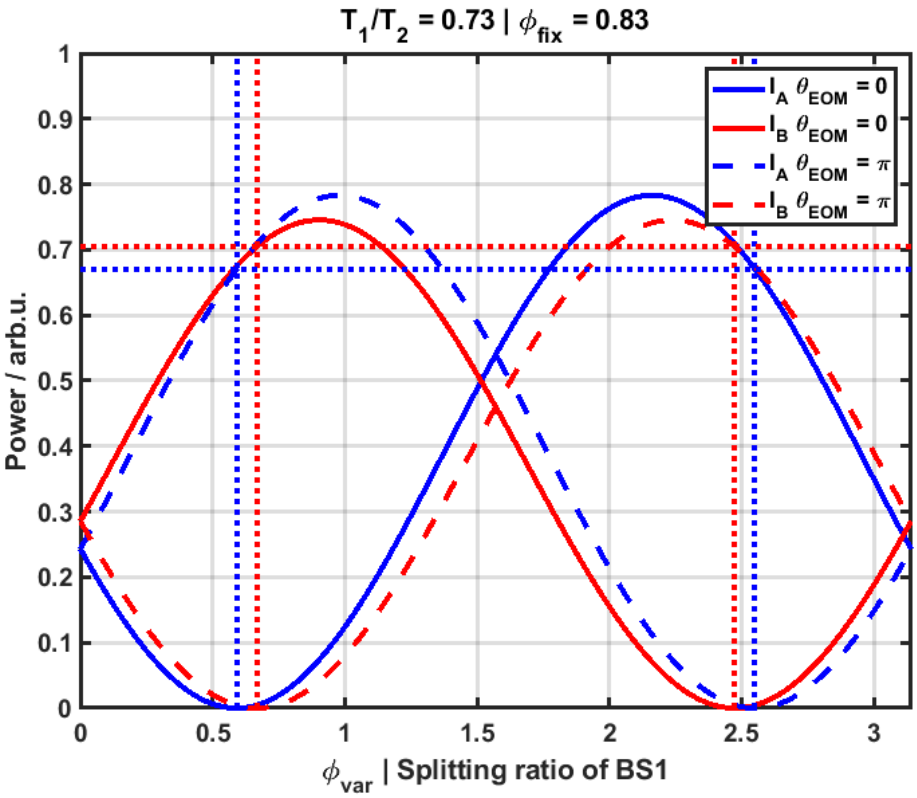

Figure 17: MZI output intensity $I_{\mathrm{A(B)}} = \|A(B)_{\mathrm{Out}}\|^2$ for $\theta_{\mathrm{DC}} = 0$. The transmission ratio $\mathrm{T}_1/\mathrm{T}_2 = 0.73$ is experimentally determined by measuring the transmittance in both arms of the MZI. The argument of the beam splitter matrix BS_2 $\phi_{\mathrm{fix}} = 0.83$ is taken from the data sheet of BS2. Note: An ideal 50:50 beam splitter would have $\phi_{\mathrm{fix}} = \frac{\pi}{4} \approx 0.79$. Vertical dotted lines mark a splitting ratio where a visibility of 1 ($I^{\mathrm{min}}_{\mathrm{A(B)}} = 0$) is reached. Horizontal dotted lines mark the corresponding power.

Figure 17 reveals that visibility of unity can only be reached for one output at a time and that contrast differs depending on the output. It is therefore crucial to monitor the output A_{Out} (towards the QD sample) while tuning BS1 for maximum visibility.

In our experiment we achieved this by first attenuating the laser pulses leaving A_{Out} and then redirecting them towards a superconducting nanowire single photon detector (SNSPD) with a time-jitter of around 27 ps. A time tagger (TT) then recorded the arrival times of single photons and the pulse-shape was reconstructed via a histogram (see figure 18). The trigger ($\mathrm{T_A}$) provided by the AWG was used to synchronise pulse generation and measurement. Figure 18 shows the recorded signal at maximum reached visibility of $V^{\mathrm{max}}_{\mathrm{A}} = 0.95(1)$ and a contrast of $C^{\mathrm{max}}_{\mathrm{A}} = 16(1)\,\mathrm{dB}$. We estimated the uncertainties by calculating the standard deviations of V and C by comparing all points that were recorded in the "Off" state of the pulse sequence to the maximum photon

count.

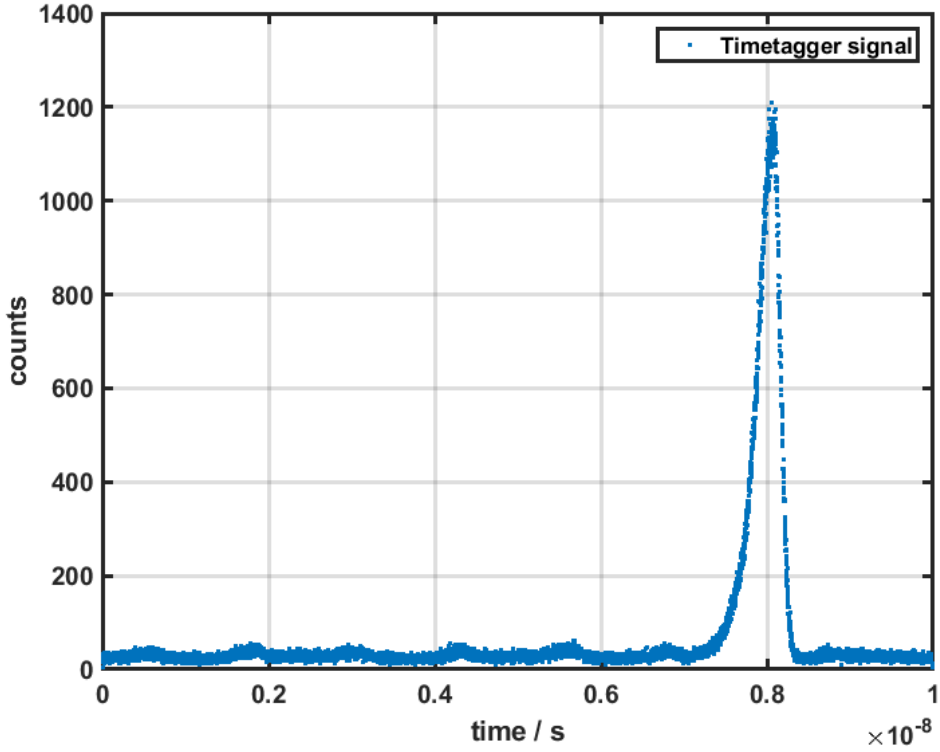

Figure 18: Recorded signal on an SNSPD of a generated pulse sequence used to tune BS1 for high visibility and contrast. A maximum visibility of $V_{\mathrm{A}}^{\mathrm{max}} = 0.95(1)$ and a contrast of $C_{\mathrm{A}}^{\mathrm{max}} = 16(1)\,\mathrm{dB}$ is reached.

Drift stabilisation

Due to thermal, acoustic and field-induced drifts in the EOM the optical setup needs to be actively stabilised. Field-induced drifts occur due to the applied voltage and subsequent current leakage across the EOM [65]. Stabilisation is achieved by sending calibration pulses through the system and mapping them onto the transfer function

$$I_{\mathrm{A}} = 1 - \cos^2\left(\frac{\theta_{\mathrm{EOM}} + \theta_{\mathrm{DC}}}{2}\right) \tag{3.7}$$

of an MZI as visualized in figure 19. In order to distinguish between excitation and calibration pulses we programmed the AWG to provide two different triggers ($\mathrm{T_A}$ and $\mathrm{T_B}$). $\mathrm{T_A}$ is timed to be centred during the excitation sequence and is sent towards the time tagger, while $\mathrm{T_B}$ relates to the calibration pulse and is used by the oscilloscope during drift stabilisation (see $\mathrm{T_A}$ and $\mathrm{T_B}$ in figure 19a). During the experiments one

calibration pulse is sent every 500 excitation pulses. The phase θ_{DC} is controlled by feeding a DC voltage into the bias tee (BT) and is stabilized to $\theta_{\mathrm{DC}} = 0$.

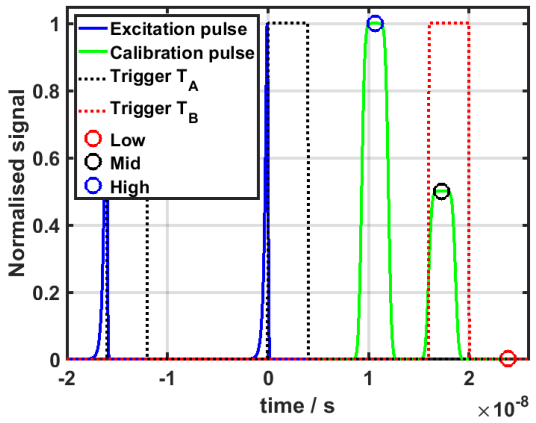

(a) Calibration pulse next to an excitation pulse. The signal intensities at **Low**, **Mid** and **High** are measured by the oscilloscope and used to determine the state of the system. Calibration pulses are triggered separately to distinguish between excitation pulse and calibration pulse.

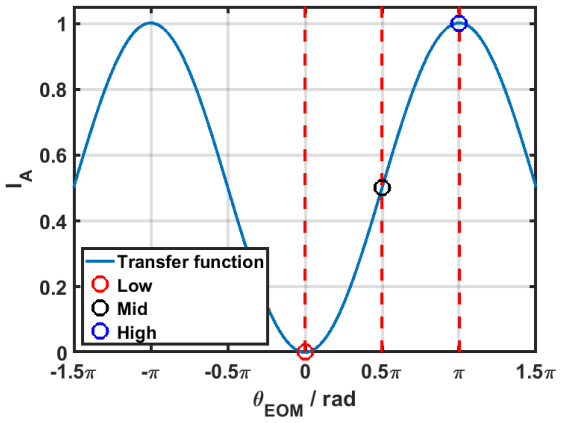

(b) Transfer function of a MZI in stable operation: $\theta_{\mathrm{DC}} = 0$. The points **Low**, **Mid** and **High** are intersections of the transfer function with the vertical dashed lines. A system where $\theta_{\mathrm{DC}} \neq 0$ has a left or right shifted transfer function.

Figure 19: Principle of the stabilisation procedure. The points **Low**, **Mid** and **High** correspond to $\theta_{\mathrm{EOM}} = 0$, $\theta_{\mathrm{EOM}} = \frac{\pi}{2}$ and $\theta_{\mathrm{EOM}} = \pi$ and are measured on the oscilloscope. Utilising equation (3.7) the current value of θ_{DC} is determined and a stabilisation algorithm calculates the necessary shift in DC voltage.

By monitoring the values of points **Low**, **Mid** and **High**, which correspond to $\theta_{\mathrm{EOM}} = 0$, $\theta_{\mathrm{EOM}} = \frac{\pi}{2}$ and $\theta_{\mathrm{EOM}} = \pi$, the current value of θ_{DC} is determined. An algorithm then calculates the necessary DC voltage shift and a micro controller (MC) in combination with a DC amplifier ($\mathrm{AMP_{DC}}$) provides a DC voltage that keeps the system in a stable operation mode $\theta_{\mathrm{DC}} = 0$.

3.1.2 Electrical setup

The heart of the electrical setup is an arbitrary waveform generator (AWG), which is able to output signals with a sample rate up to 65 GSa/s and an analogue bandwidth of 32.5 GHz. It also provides two triggers ($\mathrm{T_A}$ and $\mathrm{T_B}$) that are used to time the arrival of excitation and calibration pulses, respectively. Signals generated by the AWG are amplified via a high frequency amplifier ($\mathrm{Amp_{RF}}$) before they get combined with a DC voltage at a bias tee (BT). DC voltage is provided by a micro-controller (MC) in

combination with a home-made amplifier ($\mathrm{Amp_{DC}}$). An oscilloscope (Osc) and a photo diode ($\mathrm{D_{RF}}$) monitor the current state of the system. All used cables support frequencies greater than 26 GHz and the BT has its -3 dB point around 12 GHz.

The AWG is capable of producing arbitrary signal shapes, which allows for electrical signal correction as described in section 2.3.2.

Pulse shaping

The phase set by the EOM (θ_{EOM}) depends linearly on the applied voltage (see section 2.2). If V_π is introduced as the voltage at which $\theta_{\mathrm{EOM}} = \pi$ and operating at a stabilised point ($\theta_{\mathrm{DC}} = 0$), equation (3.7) can be rewritten as:

$$I_{\mathrm{A}} = 1 - \cos^2\left(\frac{\pi}{2V_\pi}V\right). \tag{3.8}$$

Rearranging equation (3.8) and making V and I time dependent gives an expression for the necessary applied voltage for arbitrary output intensities $I_{\mathrm{A}}(t) \in [0, 1]$.

$$V(t) = \frac{2V_\pi}{\pi}\arccos\left(\sqrt{1 - I_{\mathrm{A}}(t)}\right) \tag{3.9}$$

This allows calculating the necessary time dependent voltage $V(t)$ applied to the EOM for any given pulse shape.

In order to correct for electrical signal distortions the electrical components connecting the AWG and the EOM are characterised following the procedure described in section 2.3.2.

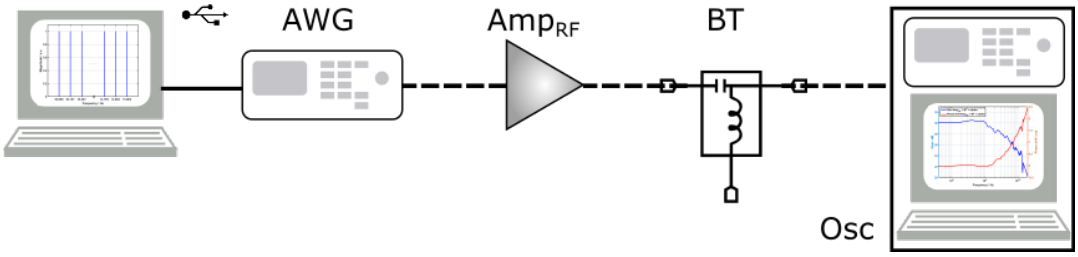

Figure 20: Setup for characterising $\mathrm{Amp_{RF}}$, BT and cables. A multi-tone measurement is performed by sending a frequency comb through the connected components and analysing the frequency response on the oscilloscope.

The AWG is capable of producing equally spaced frequency combs in which the comb teeth (frequency components) all have the same magnitude and a relative phase of zero. The frequency comb used for the multi-tone measurement consists of 100 equally spaced frequencies with a starting frequency of 50 MHz and a stop frequency of 15 GHz. These limits are chosen because the used oscilloscope has its -3 dB point around 16 GHz and frequencies smaller than 15 GHz can be assumed to be recorded lossless. The resulting Bode-diagram is shown in figure 21a.

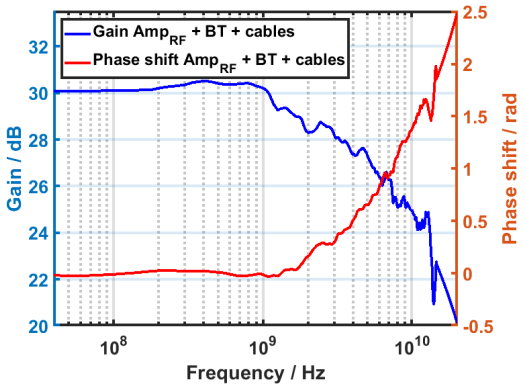

(a) Bode-diagram of all components connecting AWG and EOM. The components and measurement setup are shown in figure 20.

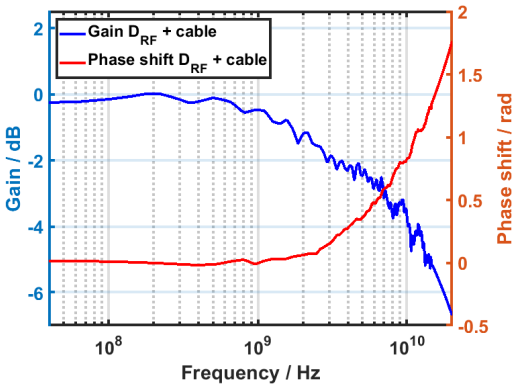

(b) Bode-diagram of D_{RF} and the cable towards the oscilloscope. This diagram is constructed by performing a multi-tone measurement on the cable and combining it with the Bode-diagram provided by the manufacturing company of D_{RF} (see appendix A.6).

Figure 21: Frequency response functions of electrical components in the experimental setup. The gain is given in dB and relates to the transmitted field amplitude. A linear shift in the electrical signal's phase, which corresponds to a delay in time, is subtracted for better readability.

3.1.3 Pulse shaping quality

Applying the method described in section 2.3.2 two different pulse shapes were created and investigated using the photo diode. The first pulse shape is of the form

$$I_R(t) = \begin{cases} \frac{1}{2}(1+\mathrm{erf}(\frac{t-\mu_1}{\sqrt{2}\sigma})) & \text{for } t<0 \\ \frac{1}{2}(1-\mathrm{erf}(\frac{t-\mu_2}{\sqrt{2}\sigma})) & \text{for } t\geq 0 \end{cases} \tag{3.10}$$

where $\mathrm{erf}(x)$ is the error function (see equation (3.11)) and is used to form smooth corners which leads to reduced high frequency components in comparison to a pure rectangular pulse. The distance $\mu_2 - \mu_1$ sets the FWHM of the pulse, while σ determines how fast the pulse's intensity rises and falls.

$$\mathrm{erf}(x) = \frac{2}{\sqrt{\pi}} \int_0^x e^{-t^2} dt \tag{3.11}$$

The second pulse shape is an asymmetric exponential pulse that is described in its non normalised form by

$$I_E(t) = (1 + \mathrm{erf}(\frac{-t+\mu_0}{a}))e^{\frac{t-\mu_0}{b}}. \tag{3.12}$$

where μ_0 sets the position of the pulse, while a and b determine the pulse's rise and fall time.

Figure 22 shows both pulses and specifies the used parameters.

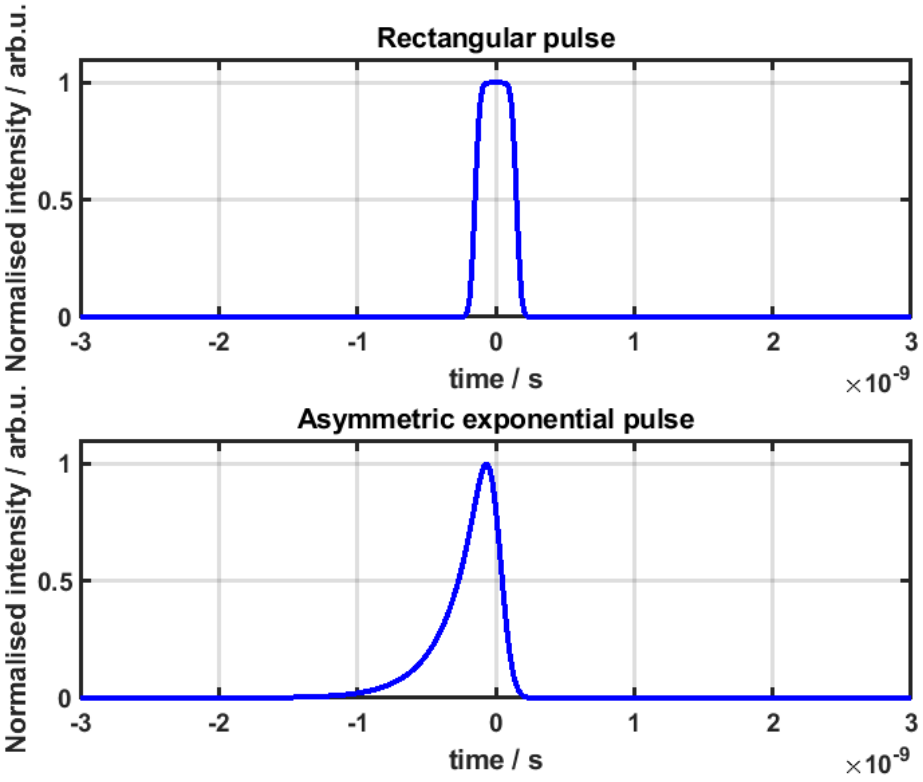

Figure 22: *Top*: Rectangular shaped pulse described by equation (3.10) with $\mu_1 = -150 \times 10^{-12}$ s, $\mu_2 = 150 \times 10^{-12}$ s and $\sigma = 45 \times 10^{-12}$ s. *Bottom*: Asymmetric exponential pulse described by equation (3.12) with $\mu_0 = 0$ s, $a = 1 \times 10^{-10}$ s and $b = 23 \times 10^{-11}$ s.

In order to view the created pulses, the frequency response of the photo diode (D_{RF}) and the cable towards the oscilloscope has to be taken into account. Figure 21b shows the Bode-diagram of those components, which is constructed by performing a multi-tone measurement on the cable and combining it with the Bode-diagram provided by the manufacturing company of D_{RF} (appendix A.6). Doing so allows simulating the expected signal and a comparison with the recorded signal is shown in figure 23.

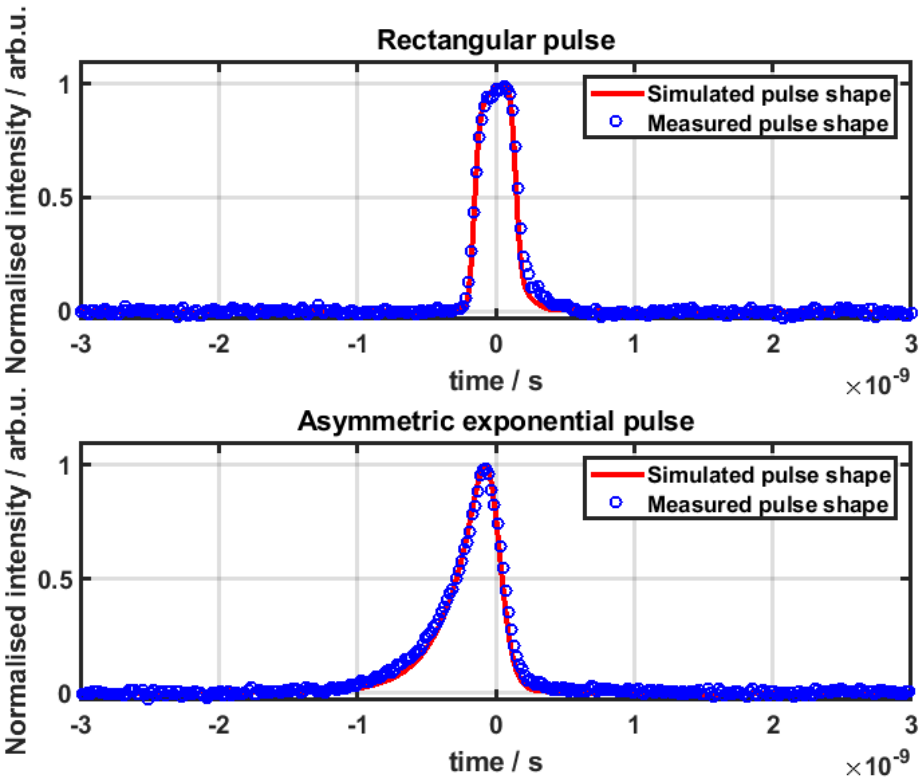

Figure 23: Comparison of the simulated pulse shapes with the recorded ones. *Top*: Rectangular pulse shape with FWHM of 300 ps. *Bottom*: Asymmetric exponential pulse shape with FWHM of 313 ps. The small deviation of the simulated pulse shapes from the pulses shown in figure 22 is due to the frequency response of the photo diode and the cable towards the oscilloscope.

Figure 23 shows that the measured pulse shape is in good agreement with the simulated expected pulse shape. The small mismatch between experimental data and the simulated curves is most likely due to the frequency response of the EOM not being perfect (constant gain) in the region of interest.

The presented pulse generation setup is capable of reliably producing arbitrary pulse shapes that are in good agreement with the expected results. Application of Fourier-methods to correct for frequency dependent distortions allow applying reliable phase shifts using the EOM. The use of a variable beam splitter to compensate for different losses in the two arms of the MZI allows a maximum visibility of $V_{\mathrm{A}}^{\mathrm{max}} = 0.95(1)$ and a contrast of $C_{\mathrm{A}}^{\mathrm{max}} = 16(1)\,\mathrm{dB}$ to be reached. After generation the pulses are fibre-coupled into a PM-fibre and sent towards the QD setup.

3.2 Quantum dot setup

To verify the usability of the pulse shaping setup, it was tested by generating Rabi oscillations on an existing QD setup. The QD under investigation is embedded in a nanowire structure and was grown by Dan Dalacu and others at the National Research Council of Canada (Ottawa) via selective-area vapour-liquid-solid growth [66–68]. A defect of InAsP surrounded by InP acts as the QD and is accompanied by another QD close to it, such that they interact and form a QD-molecule, as shown in the schematic drawing of figure 24a. The nanowires on the sample were imaged by a scanning electron microscope (SEM) and one representative image is shown in figure 24b.

Excitation light is coupled into the nanowire from the top. The nanowire acts as a waveguide and an antenna, which emits into a well-defined spatial mode (pink cone in figure 24a). A schematic view of the setup and light paths is presented in figure 25.

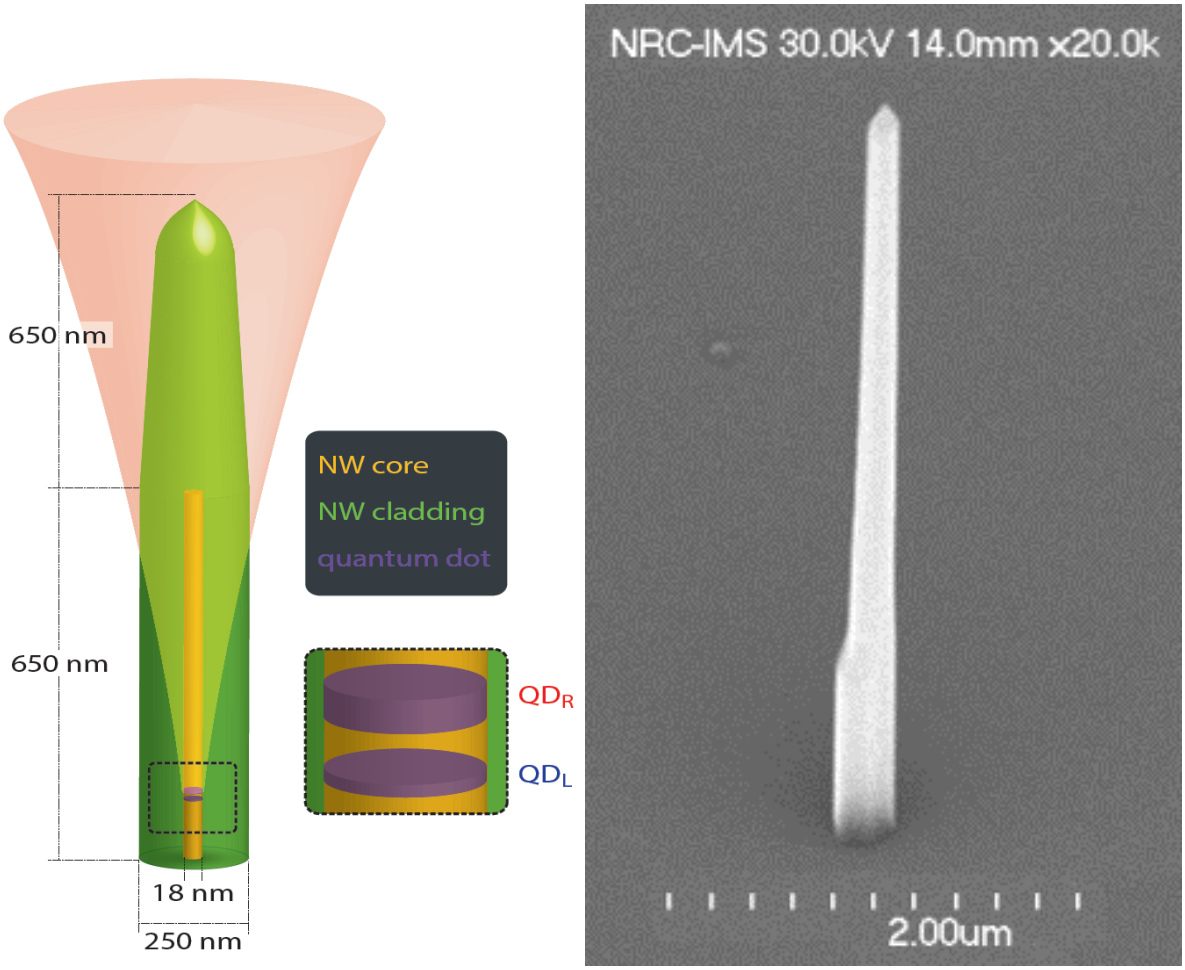

(a) Schematic of the used nanowire samples. Two QDs, QD_R and QD_L, are formed in the nanowire core during the growth process [68]. The nanowire favours an emission mode parallel to its growth axis as illustrated by the pink cone.

(b) SEM picture of a representative nanowire on the sample.

Figure 24: Nanowire structure with embedded QDs. The two QDs interact with each other and can act as a QD-molecule.

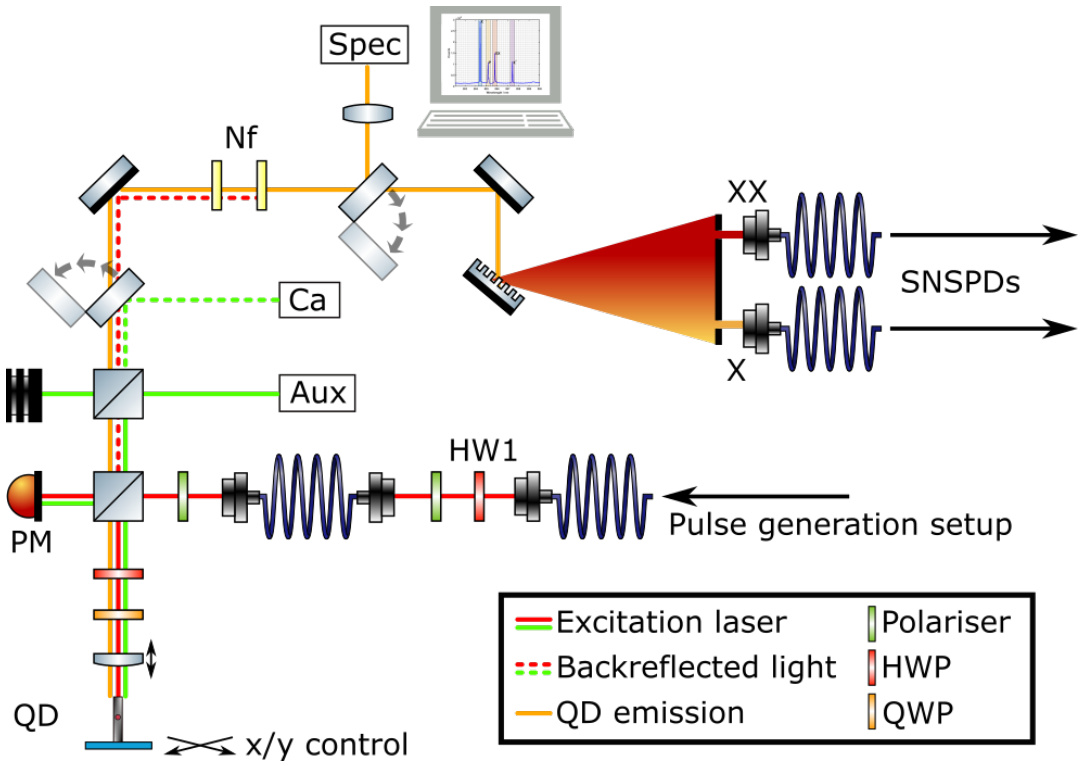

Figure 25: QD experiment. Excitation pulses generated by the MZI pulse-shaper (see section 3.1) are fibre-coupled into the QD setup (red line). Optical power is controlled via a motorized half wave plate (HW1) and a polariser. Both beam splitters in the setup transmit 90% of the light's intensity, a powermeter (PM) measures the CW equivalent power and the power sent towards the QD is estimated from the splitting ratio. A combination of a motorised quarter wave plate (QWP) and a motorised half wave plate (HWP) controls the final polarisation state of the excitation pulse. Excitation light is focused onto the QD sample, whose lateral position is controlled via a piezo-actuated translation stage. Photons emitted from the QD pass through two notch filters (Nf) that suppress back-reflected pump photons before they are sent to either a spectrometer (Spec) or are separated in energy by a grating for further analysis (orange line). The latter spatially separates the X and XX photons, which are then fibre-coupled towards the SNSPDs. An auxiliary input (Aux) is used to couple an extra laser source into the setup for above band excitation (green line). An LED illumination source can also be coupled in via Aux and a camera (Ca) records the reflected light to image the sample. An extensive component list can be found in table 3.

During all experiments a rectangular pulse shape as depicted in the top of figure 22 was used. The FWHM of the pulses was 500 ps and the repetition rate was set to

100 MHz, i.e. one pulse every 10 ns. This pulse duration was chosen because trials with shorter pulses were not able to transmit enough energy through the setup into the sample without exceeding the damage threshold of the EOM. This is mainly due to the high transmission (90%) of the beam splitters and could be reconsidered in future QD setups.

Table 3: Components of the QD setup depicted in figure 25.

Component	Abbreviation	Manufacturer	Model/Sample #
Quantum dot	QD	Dan Dalacu et al. [66]	CBE14-041-111
Single photon detector	SNPD	Single Quantum	Eos 720 CS
Spectrometer	Spec	Princeton Instruments	SP2750
Powermeter	PM	Thorlabs	PM16-130
Notch filters	Nf	OptiGrate	BNF-902(907)-OD3-12.5
Camera	Ca	Watec	WAT-902H Ultimate

3.2.1 Coherent excitation of the biexciton

In order to use the QD as a photon-pair source the $|XX\rangle$ state is excited via a two-photon resonant process, which results in the emission of two energy separated photons, as discussed in section 2.1.4. To do so in a deterministic fashion Rabi-oscillations are utilised and the application of a π-pulse results in a reliable preparation of the $|XX\rangle$ state.

First we investigated the frequency spectrum of the QD sample using the spectrometer (Spec), which has a wavelength accuracy of $\Delta\lambda = \pm 0.1$ nm. After identifying the corresponding emission energies of the X and XX photons the pump laser's wavelength was tuned to their arithmetic mean (see figure 26) so as to fulfil the condition for coherent excitation of the $|XX\rangle$ state.

We found the emission wavelengths to be centred at $\lambda_X = 894.41$ nm and $\lambda_{XX} = 895.78$ nm and, as a result, set the center wavelength of the laser source to $\lambda_P = 895.36$ nm. The detected photon counts were integrated over a 0.4 nm window, centred at the peaks of the QD emission lines (shaded regions in figure 26). A third emission line corresponding to the formation of a trion (X^*) was located at 897.45 nm and back-reflected pump photons were also present in the recorded spectrum (P).

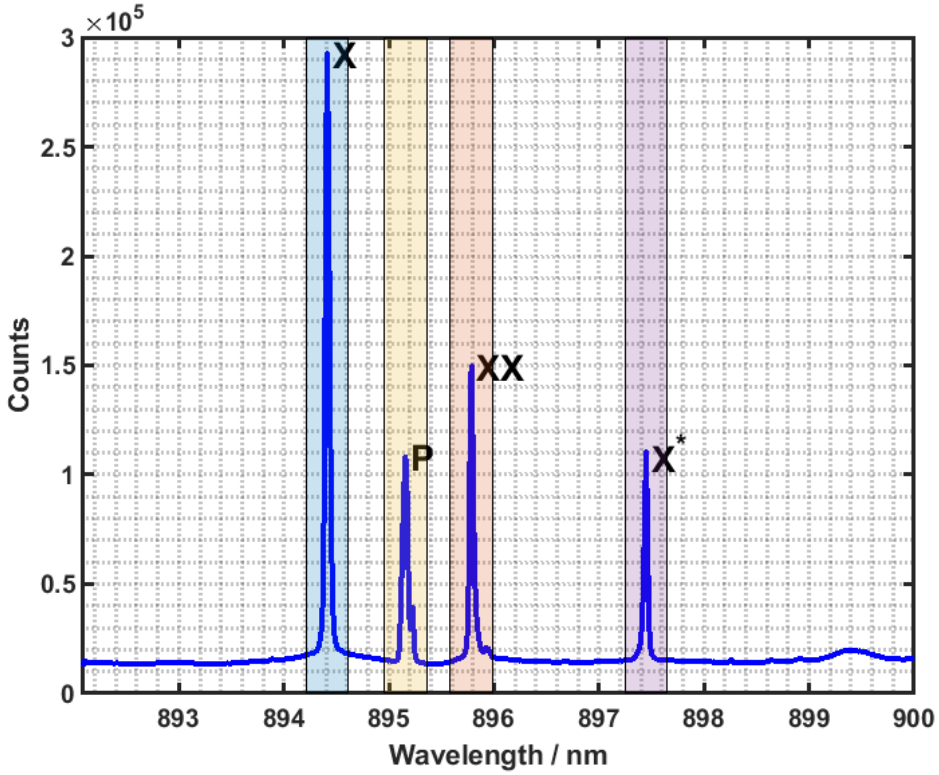

Figure 26: Emission spectrum of the QD sample. The X emission energy is centred around 894.41 nm, XX photons are found at 895.78 nm and a trion (X^*) emission is observed at 897.45 nm. Back-reflected pump photons (P) are suppressed by the two notch filters (Nf) in the setup but residual photons are also captured with a maximum at 895.16 nm. The shaded areas indicate the region over which the recorded counts are integrated.

A motorized half-wave plate (HW1 in figure 25) in combination with a polariser was used to tune the arriving power of the excitation pulses and CW equivalent power was recorded by a powermeter (PM) in front of the QD sample. By scanning through different powers we observed Rabi oscillations by recording the emitted photon number of the $|XX\rangle \rightarrow |X\rangle$ transition for a fixed duration of 1 s per excitation power.

Two-photon resonant Rabi oscillations in the dipole approximation depend on Ω_0^2, which is linearly proportional to optical power (Ω_0 is the coupling strength in the dipole approximation and is linearly proportional to the electric field, see equation (2.44)). This leads to oscillations of the form:

$$C = C_\pi \sin^2\left(\frac{P_{\mathrm{CW}}}{2P_\pi}\pi\right) \tag{3.13}$$

with C being the recorded photocount, C_π the maximum photocount reached, P_{CW} the

recorded CW equivalent power at the PM and P_π the power equivalent to a π-pulse. A rise in P_{CW} corresponds to an increase of pulse area, which is achieved by rotating HW1 in front of a polariser.

The integrated peak intensities for X, XX, X* and P are shown in figure 27 for increasing excitation power.

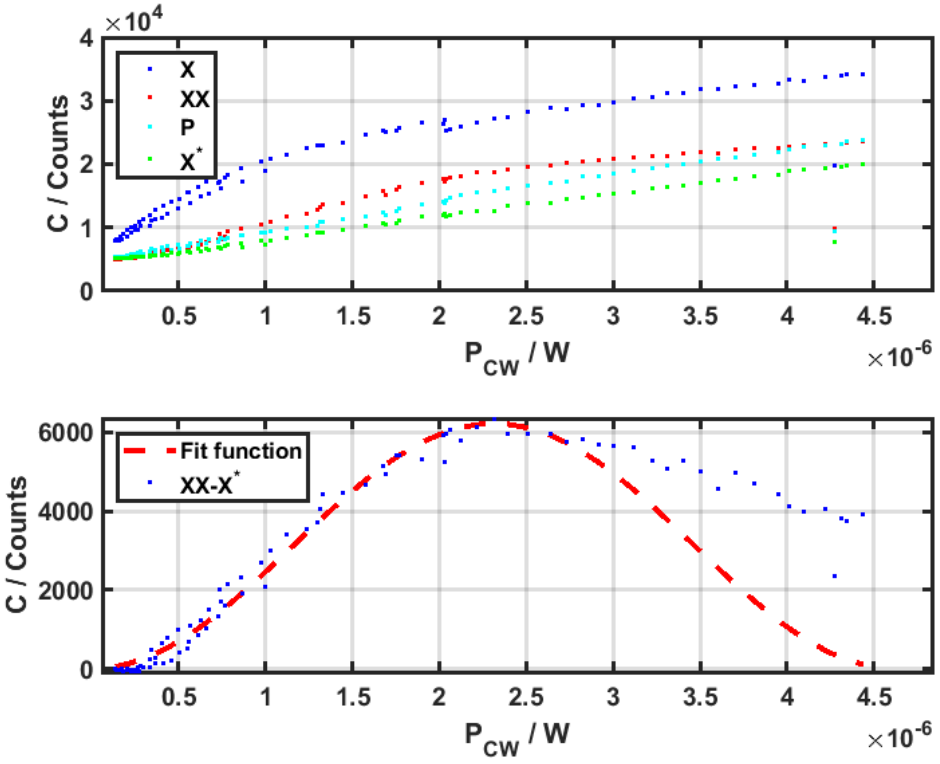

Figure 27: *Top*: Integrated peak areas of recorded photon counts for X (blue), XX (red), X* (green) and P (cyan) wavelengths. *Bottom*: XX intensity corrected for incoherent processes (XX-X*) and fit function equation (3.13) with $C_\pi = 6221(5)$ and $P_\pi = 231(2) \times 10^{-8}$ W. Error estimation is the standard deviation provided by the fit-routine.

The recorded intensities of the X and XX emissions do not show pure Rabi oscillations as seen in the top plot of figure 27. This suggests that there are incoherent processes that populate the $|XX\rangle$ and $|X\rangle$ states. These are attributed to the long pulse duration, which is at the order of the state's lifetimes and lead to natural decoherence of the Rabi oscillations. Arguing that the same incoherent processes lead to a population of the trion state, we corrected the XX photon count by subtracting the trion photon count, multiplied by a scaling factor. This correction reveals Rabi oscillations of the $|XX\rangle$ state as seen in the bottom plot of figure 27. The extracted fit parameters of equation (3.13)

are $C_\pi = 6221(5)$ and $P_\pi = 231(2) \times 10^{-8}$ W. Error estimation is the standard deviation provided by the fit-routine.

This assumption of incoherent processes is supported by fitting a polynomial function of the form

$$I = a \cdot P_{\mathrm{CW}}^{b} + c \tag{3.14}$$

to the low P_{CW} region of the recorded intensities for X and XX photons. The parameter b determines the polynomial order of the rise in emission intensity. For a two-photon process $b = 2$ (see chapter 1 of [69]). In a purely coherent process both slopes should be of order $\sin^2(P_{\mathrm{CW}}) \approx P_{\mathrm{CW}}^2$, since they are a product of the same excitation process. This is not the case as can be clearly seen in figure 28.

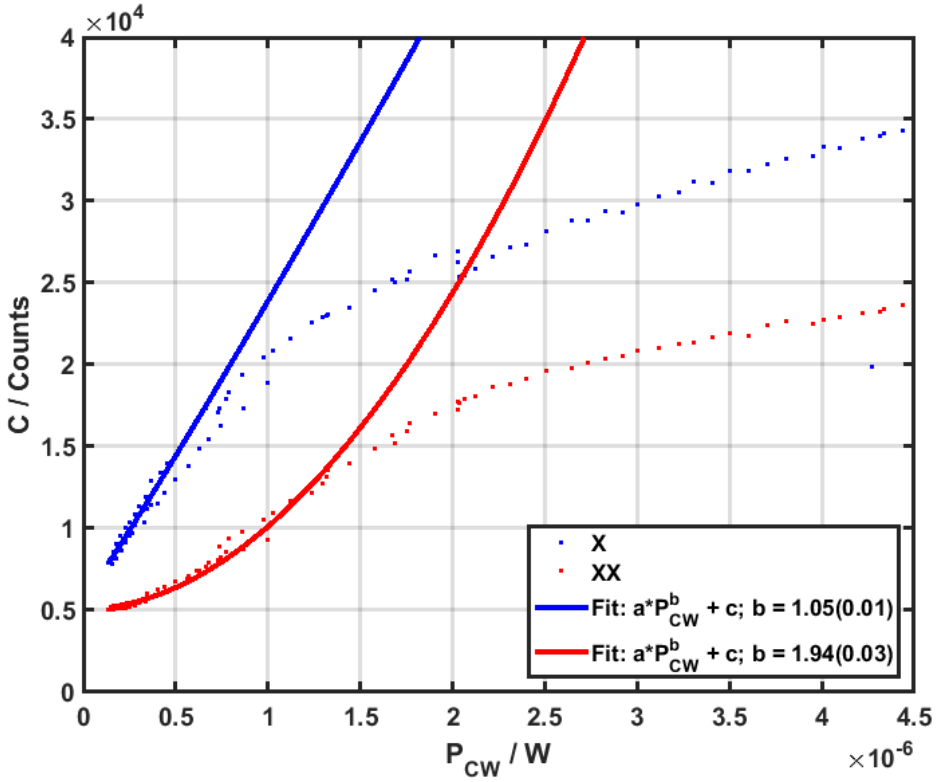

Figure 28: Slopes of the recorded intensities for X and XX photons. While the XX intensity rises almost quadratically ($b = 1.94(0.03)$) the X photons exhibit a more linear behaviour ($b = 1.05(0.01)$) which indicates a direct (single-photon) excitation into the $|X\rangle$ state. Error estimation is provided by the fit-routine and corresponds to the standard deviation.

Coherent excitation of the XX state on the same sample has been achieved by the use of a pulsed laser source (Spectra-Physics, Tsunami) with a pulse repetition rate (PRR) of 80 MHz and a pulse width of FWHM = 85 ps. Data from this measurement is

presented in figure 29 and is included as a benchmark for comparison to the technique presented in this thesis using pulse shaping from a MZI pulse generator. Note that the normalised state population exhibits a damped oscillation which converges towards one half. This is in agreement with QD models that include phonon-induced dephaseing as discussed in section 2.4.3 and [58].

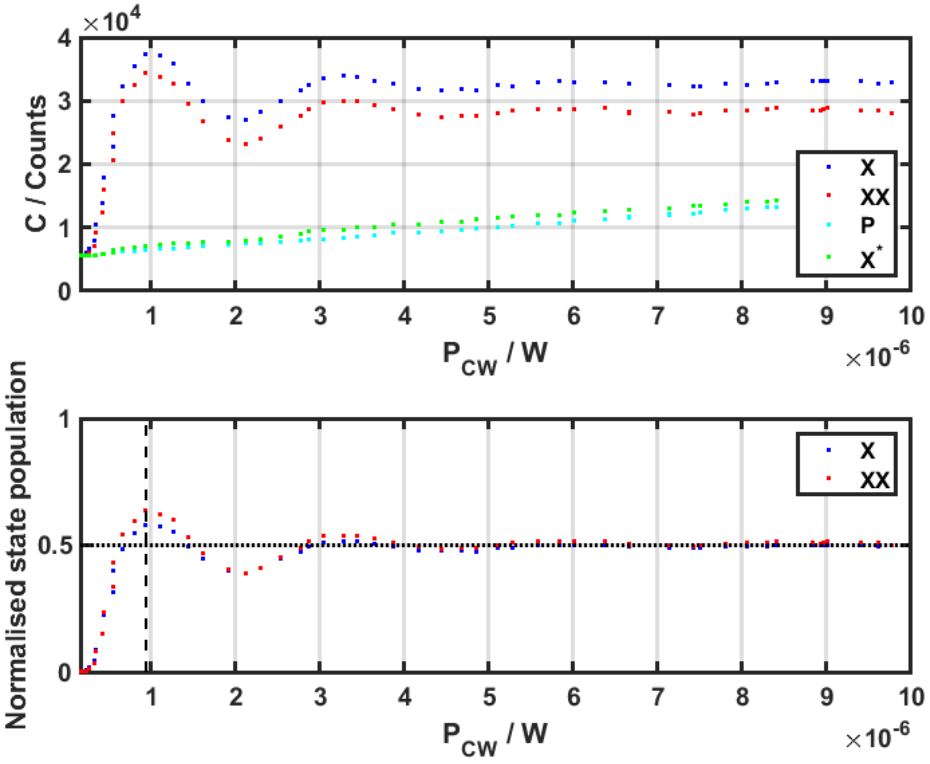

Figure 29: Excitation via a pulsed laser source (Spectra-Physics, Tsunami, PRR: 80 MHz, FWHM: 85 ps). *Top*: Integrated peak intensities of recorded photon counts for X, XX, X* and pump light (P) wavelengths. *Bottom*: Normalised state population of the $|XX\rangle$ and $|X\rangle$ states. Fitting the model of equation (3.13) reveals a maximum population probability of 0.58(1) for X and 0.64(1) for XX after a π-pulse of strength $P_\pi = 94(5) \times 10^{-8}$ W(dashed line). Error estimation is the standard deviation provided by the fit-routine. Convergent behaviour towards 0.5 is seen for larger pulse areas, which is in agreement with the models presented in [58].

This shows that coherent control of the XX state can be achieved by the use of suitable short laser pulses and indicates that QDs can be used as deterministic photon-pair sources, on which state rotations can be performed by the use of a laser pulse of appropriate length and intensity.

The pulses created by the fibre coupled MZI pulse generation setup (section 3.1) were not able to produce exclusively coherent excitation into the $|XX\rangle$ state. The coherent component (Rabi oscillations) became visible only after subtracting the incoherent contribution estimated from the emitted X^* photons (see figure 27). Due to the limited available pulse energy the bottom plot of figure 27 shows only one peak. This suggests that the current pulse generation setup needs to be adapted in order to be used as a reliable source for excitation pulses (see section 3.3).

3.2.2 Investigating the life time of excited states

As a second measure to verify the pulse generation scheme presented in this thesis the lifetimes of the involved electronic states were investigated using pulses created by the pulse generation setup. Time resolved photoluminescence spectroscopy was performed by exciting the QD sample, separating the emitted photons in their wavelengths and counting them on SNSPDs. Their time of arrival was recorded by a time tagger and was synchronised to the excitation pulses via the trigger channel T_A. As mentioned in section 3.2.1 the excitation process showed a mixture of coherent and incoherent behaviour and the model derived in section 2.5 can only be applied to some sections of the recorded data.

We expect the emission of XX photons to show an exponential behaviour as described in equation (2.50). The recorded data presented in figure 30 shows a bi-exponential decay for the $|XX\rangle \rightarrow |X\rangle$ transition and fitting the model to the corresponding regions extracts two different lifetimes τ_{fast} and τ_{slow}. This bi-exponential behaviour is likely a result of the long excitation pulse itself in combination with residual laser intensity after the excitation pulse leading to stimulated emission from the $|XX\rangle$ state. A shoulder is visible in the XX emission around 1×10^{-9} s, which is assigned to two different excitation processes. First the two-photon excitation $|0\rangle \rightarrow |XX\rangle$ is the most likely to happen. After $\approx 1 \times 10^{-9}$ s the $|X\rangle$ state is populated via an undesired single photon excitation $|0\rangle \rightarrow |X\rangle$ and excitation into the $|XX\rangle$ state happens via the transition $|X\rangle \rightarrow |XX\rangle$. The observed shoulder is a result of the transition between those excitation channels.

The transition $|X\rangle \rightarrow |0\rangle$ shows a large incoherent behaviour and a lifetime τ_{single} is assigned via an exponential fit. This decay is expected to be a result of directly populating the $|X\rangle$ state via a single-photon process. Utilising the extracted parameter for the maximum occupation number N_0 and the mean of τ_{fast} and τ_{slow} allows identifying the photons that correspond to the coherent decay $|XX\rangle \rightarrow |X\rangle \rightarrow |0\rangle$. Fitting equation (2.50) to the identified region extracts a lifetime τ_{double} that is in agreement with the model of two coupled energy levels where one feeds into the other (see section 2.5).

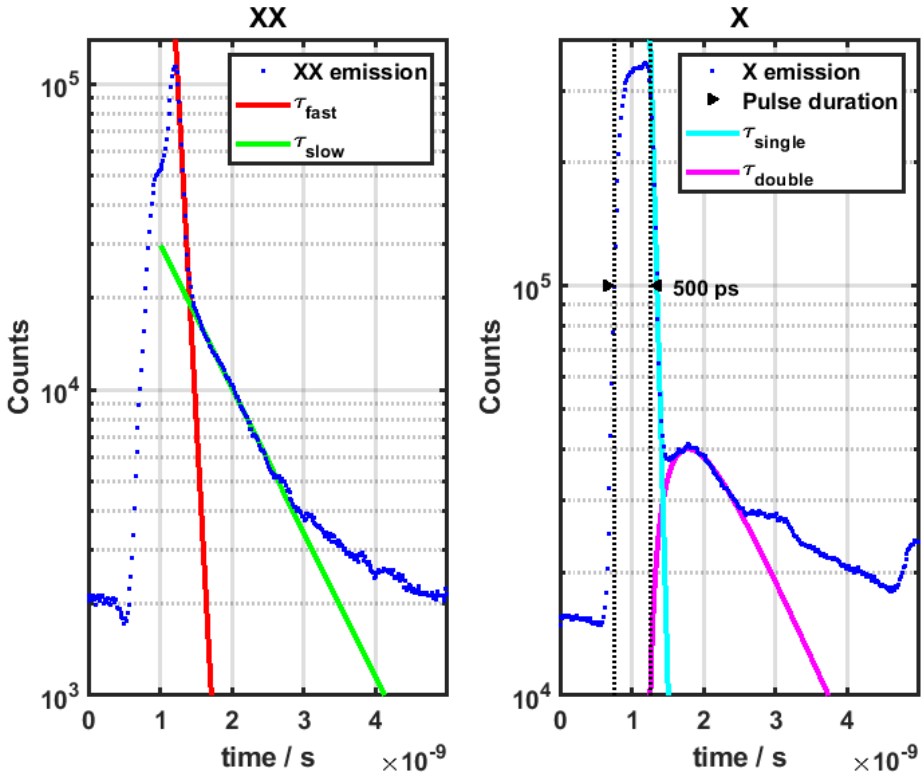

Figure 30: Time resolved photoluminescence spectroscopy for CW equivalent excitation power of 7.5 µW. *Left*: Collected photons at the XX wavelength. A bi-exponential behaviour is observed and indicated by two exponential fits (red and green). *Right*: Collected photons at the X wavelength. The total count of X photons is more than five times the total number of counted XX photons which again indicates an incoherent single-photon excitation channel into the $|X\rangle$ state. An exponential behaviour is fitted into the data and an incoherent lifetime (τ_{single}) is assigned to that decay (exponential fit in cyan). The peak right after the incoherent emission is a result of coherent excitation and the model of section 2.5 is used to assign a coherent lifetime (τ_{double}, fit in magenta). The imprint of the excitation pulse shape (rectangular pulse, FWHM: 500 ps) is clearly seen in the exciton emission which also hints at incoherent single-photon excitation.

The measurement was repeated for different CW equivalent excitation powers. The extracted life time values are presented in table 4 and are displayed in figure 31. Uncertainties are calculated by the fit-routine and are the estimated standard deviations. At lower CW equivalent powers the peak assigned to the coherent decay $|XX\rangle \rightarrow |X\rangle \rightarrow |0\rangle$ is less prominent and the fitting routine struggles to find a well-estimated value for τ_{double}. A previous lifetime measurement on the same sample resulted in two lifetimes

$\tau_{XX} = 1.5(2)\,\text{ns}$ and $\tau_X = 3.1(5)\,\text{ns}$ (supplementary material of [70]). These values differ from our extracted lifetimes by roughly one order of magnitude, which is most likely due to the different excitation scheme utilizing a CW pump.

Table 4: Lifetimes: τ_{fast}, τ_{slow} and τ_{single} are obtained by fitting a single exponential decay into the measured data. τ_{double} is extracted from the data by fitting the model described in equation (2.50). Error estimation is the standard deviation provided by the fit-routine.

P_{CW} / µW	τ_{fast} / ps	τ_{slow} / ps	τ_{single} / ps	τ_{double} / ps
2.0	204(9)	609(2)	102(5)	681(155)
2.5	180(8)	584(3)	90(3)	1063(62)
3.0	170(8)	601(2)	84(2)	1088(55)
3.7	160(8)	642(4)	86(2)	1661(62)
4.3	142(6)	639(4)	77(2)	1428(63)
5.0	133(6)	676(3)	72(1)	1333(68)
6.0	119(5)	734(3)	68(1)	1181(67)
6.5	115(5)	809(5)	67(1)	948(78)
7.0	110(5)	905(6)	69(2)	1122(79)
7.5	101(5)	919(7)	68(2)	340(22)
8.0	97(4)	954(9)	65(1)	335(22)

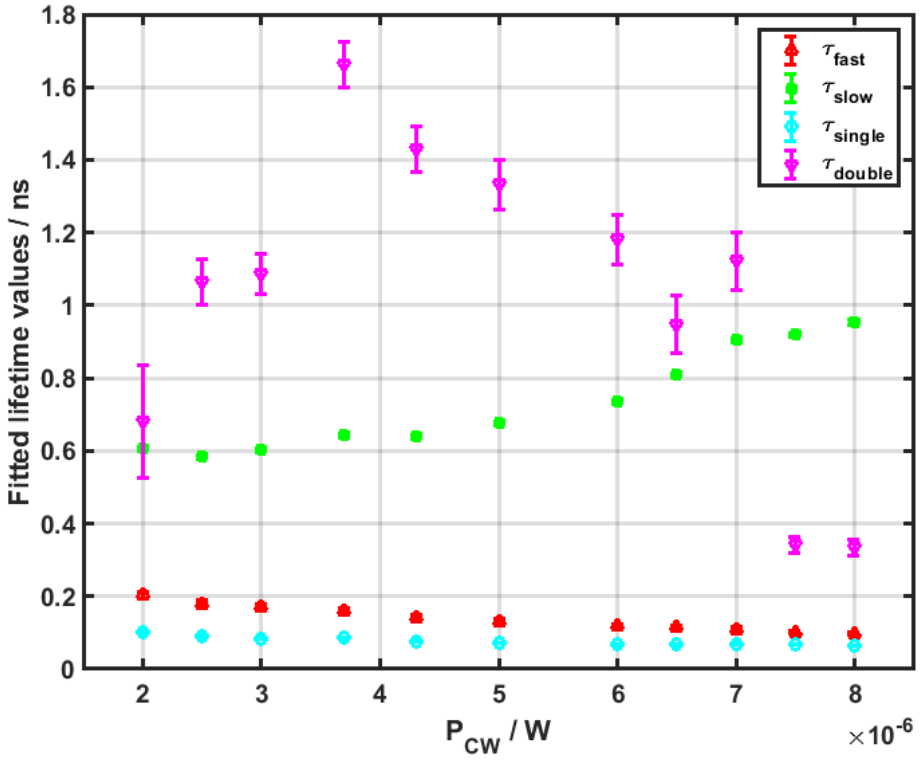

Figure 31: Extracted lifetimes for different CW equivalent excitation powers. The errorbars of τ_{fast},τ_{slow} and τ_{single} are smaller than the marker size. Uncertainties are the standard deviations resulting from the fitting routine and are found in table 4.

Exciting the QD via pulses generated in the pulse generation setup and investigating the lifetimes of electronic states in the QD sample reveals that the transition $|XX\rangle \rightarrow |X\rangle$ occurs at two different time scales (τ_{fast}, τ_{slow}, red and green fit in figure 31). This bi-exponential behaviour is expected to be due to spontaneous emission induced by a residual laser field after the excitation pulses. The emission out of the $|X\rangle$ state shows a clear imprint of the excitation pulse which indicates that direct single-photon excitation took place during the excitation scheme. An exponential fit is used to extract a corresponding lifetime (τ_{single}, cyan fit). Utilising the parameters extracted from the XX emission, the peak indicated by the magenta fit is expected to be a result of the transition $|XX\rangle \rightarrow |X\rangle \rightarrow |0\rangle$ and the model of equation (2.50) is used to extract a corresponding lifetime (τ_{double}).

3.3 Future improvements on the pulse generation setup

The pulse shaping quality of the presented fibre coupled MZI pulse shaper is in good agreement with the simulations and pulse shapes can be reliably produced via the MZI setup (see section 3.1.3). However, preparation of the $|XX\rangle$ state occurred as a mixture of coherent and incoherent excitation. It is expected that residual laser intensity during the "Off" state of the excitation pulses is one cause for the incoherent behaviour. In order to tune the setup to have both, a high contrast and high visibility, the current setup relies on a variable beam splitter to compensate for different losses in the two arms of the MZI. This is achieved by manually adjusting the splitting ratio via a micrometer screw and is difficult to control. The beam splitter also shows hysteresis and mechanical relaxation which leads to unreproducible results. A better way to tune for high visibility would be to replace the variable by a fixed beam splitter and introduce an electrically controlled attenuator into the currently device free arm of the MZI. This would allow purely electrical control of the pulse generation setup and could also be used in an automated optimisation protocol. Another advantage would be that no part of the setup would have to be manually accessible and it could be decoupled from the environment to a greater extent, improving operation stability.

Another cause of the incoherent excitation behaviour is that the current system relies on rather long (500 ps) pulses in order to transmit enough energy into the QD sample. Implementing a semiconductor optical amplifier (SOA) after the MZI setup would allow for higher optical power in shorter pulses without exceeding the damage threshold of the EOM.

4 Summary, discussion and outlook

In this section, the results of the performed experiments are discussed and an outlook on possible future experiments is presented.

The goal of this thesis was to build and characterise a fibre-coupled, electrically controlled MZI in order to create arbitrary laser pulse shapes and sequences. Those pulses were then sent towards a QD to coherently excite the $|XX\rangle$ state and characterise the subsequent photon emission (see section 3).

Utilising Fourier methods to correct for electrical signal distortion resulted in the reliable generation of optical pulse shapes that were in good agreement with the simulations (see figure 23). In the current system a maximum visibility of $V^{\max} = 0.95(1)$ accompanied by a contrast of 16(1) dB was reached. We expect to be able to improve these values in the future by adapting the pulse generation setup as discussed in section 3.3.

A QD sample embedded in a nanowire structure was excited into its $|XX\rangle$ state via two-photon resonant excitation and the emitted photons were analysed by a spectrometer and superconducting nanowire single photon detectors. The use of a pulsed laser source demonstrated Rabi-oscillations between the ground state and the $|XX\rangle$ state and application of a π-pulse of strength $94(5) \times 10^{-8}$ W resulted in a maximum state population probability of 0.64(1) for the $|XX\rangle$ state and 0.58(1) for the $|X\rangle$ state (see figure 29). This shows that state manipulation in a QD can be achieved by the use of laser pulses and QDs can be used as a controllable single-photon (photon-pair) source needed for the implementation of optical quantum computation [8].

Replacing the pulsed laser source with the fibre coupled MZI pulse shaper did not show purely coherent excitation but introduced incoherent excitation processes due to the need for pulse widths that were longer than the lifetimes of the electronic states, resulting in natural dephaseing. Correcting for these incoherent processes revealed Rabi-oscillations and a maximum emission intensity was recorded after the application of a π-pulse of strength $231(2) \times 10^{-8}$ W (see figure 27).

We performed time-resolved photoluminescence spectroscopy on the emitted photons after excitation via the MZI pulse generation setup and thus investigated the lifetimes of the $|XX\rangle$ and $|X\rangle$ states. Because the transition $|XX\rangle \rightarrow |X\rangle$ showed a bi-exponential behaviour we assigned two different lifetimes (τ_{fast} and τ_{slow}). This bi-exponential decay is expected to be a result of the long excitation pulses (500 ps), whose duration is at the order of the extracted lifetimes and leads to natural dephasing of the states. Another reason for the bi-exponential decay could be due to residual laser intensity after the excitation pulses leading to stimulated emission from the $|XX\rangle$ state. This assumption is supported by the decrease of τ_{fast} for higher excitation powers, as seen in figure 31. Photons emitted from the $|X\rangle$ state showed clear evidence for undesired single-photon excitation, i.e. a photon count that was more than five times higher than the XX photon count and had the shape of the excitation pulse. Although most photons emitted out of the $|X\rangle$ state could be assigned to a single-photon excitation process, we identified a

region that corresponds to the transition $|XX\rangle \rightarrow |X\rangle \rightarrow |0\rangle$ by the use of the model derived in section 2.5. All extracted lifetimes can be found in table 4 and figure 31. Comparison with a previous lifetime measurement on the same sample showed two lifetimes $\tau_{\mathrm{XX}} = 1.5(2)\,\mathrm{ns}$ and $\tau_{\mathrm{X}} = 3.1(5)\,\mathrm{ns}$ which are roughly an order of magnitude longer than our values (supplementary material of [70]). This is most likely to the different excitation scheme utilizing a CW pump.

The presented fibre-coupled MZI pulse shaper is capable of reliably producing arbitrary pulse shapes with good accuracy. However, it was not capable of exciting the QD in a purely coherent way. This is attributed to the long pulse duration which is at the order of the state's lifetimes and residual laser light during the "Off" state of the MZI and could be improved by the means presented in section 3.3. Resolving this issue would enable the creation of computational useful photon states like cluster states or higher dimensional time-bin entangled photon-pairs, using the pulse shaping setup described in this thesis [71–73].

Similar to [74], the precise electrical control of a phase-shifting EOM, achieved in this thesis, could also be utilised to perform phase shifting operations on single photons and could demonstrate a "photon sorter" for time-bin entangled photons.

References

[1] P. W. Shor, "Algorithms for quantum computation: Discrete logarithms and factoring," in *Proceedings 35th annual symposium on foundations of computer science*, pp. 124–134, Ieee, 1994.

[2] L. K. Grover, "Quantum mechanics helps in searching for a needle in a haystack," *Physical review letters*, vol. 79, no. 2, p. 325, 1997.

[3] L.-M. Duan, J. I. Cirac, and P. Zoller, "Geometric manipulation of trapped ions for quantum computation," *Science*, vol. 292, no. 5522, pp. 1695–1697, 2001.

[4] Y. Nakamura, Y. A. Pashkin, and J. Tsai, "Coherent control of macroscopic quantum states in a single-Cooper-pair box," *nature*, vol. 398, no. 6730, p. 786, 1999.

[5] J. Wrachtrup, S. Y. Kilin, and A. Nizovtsev, "Quantum computation using the 13 C nuclear spins near the single NV defect center in diamond," *Optics and Spectroscopy*, vol. 91, no. 3, pp. 429–437, 2001.

[6] D. Loss and D. P. DiVincenzo, "Quantum computation with quantum dots," *Physical Review A*, vol. 57, no. 1, p. 120, 1998.

[7] A. Y. Kitaev, "Unpaired Majorana fermions in quantum wires," *Physics-Uspekhi*, vol. 44, no. 10S, p. 131, 2001.

[8] J. L. O'brien, "Optical quantum computing," *Science*, vol. 318, no. 5856, pp. 1567–1570, 2007.

[9] T. Rudolph, "Why I am optimistic about the silicon-photonic route to quantum computing," *APL Photonics*, vol. 2, no. 3, p. 030901, 2017.

[10] A. Politi, J. C. Matthews, and J. L. O'brien, "Shors quantum factoring algorithm on a photonic chip," *Science*, vol. 325, no. 5945, pp. 1221–1221, 2009.

[11] P. G. Kwiat, J. Mitchell, P. Schwindt, and A. White, "Grover's search algorithm: an optical approach," *Journal of Modern Optics*, vol. 47, no. 2-3, pp. 257–266, 2000.

[12] M. D. Eisaman, J. Fan, A. Migdall, and S. V. Polyakov, "Invited review article: Single-photon sources and detectors," *Review of scientific instruments*, vol. 82, no. 7, p. 071101, 2011.

[13] J. Zheng, C. Zhang, and R. M. Dickson, "Highly fluorescent, water-soluble, size-tunable gold quantum dots," *Physical Review Letters*, vol. 93, no. 7, p. 077402, 2004.

[14] N. R. Panyala, E. M. Peña-Méndez, and J. Havel, "Gold and nano-gold in medicine: overview, toxicology and perspectives.," *Journal of Applied Biomedicine (De Gruyter Open)*, vol. 7, no. 2, 2009.

[15] D. M. Zajac, A. J. Sigillito, M. Russ, F. Borjans, J. M. Taylor, G. Burkard, and J. R. Petta, "Resonantly driven CNOT gate for electron spins," *Science*, vol. 359, no. 6374, pp. 439–442, 2018.

[16] T. Watson, S. Philips, E. Kawakami, D. Ward, P. Scarlino, M. Veldhorst, D. Savage, M. Lagally, M. Friesen, S. Coppersmith, *et al.*, "A programmable two-qubit quantum processor in silicon," *Nature*, vol. 555, no. 7698, p. 633, 2018.

[17] M. Veldhorst, C. Yang, J. Hwang, W. Huang, J. Dehollain, J. Muhonen, S. Simmons, A. Laucht, F. Hudson, K. M. Itoh, *et al.*, "A two-qubit logic gate in silicon," *Nature*, vol. 526, no. 7573, p. 410, 2015.

[18] F. Martins, F. K. Malinowski, P. D. Nissen, E. Barnes, S. Fallahi, G. C. Gardner, M. J. Manfra, C. M. Marcus, and F. Kuemmeth, "Noise suppression using symmetric exchange gates in spin qubits," *Physical review letters*, vol. 116, no. 11, p. 116801, 2016.

[19] M. Reed, B. Maune, R. Andrews, M. Borselli, K. Eng, M. Jura, A. Kiselev, T. Ladd, S. Merkel, I. Milosavljevic, *et al.*, "Reduced sensitivity to charge noise in semiconductor spin qubits via symmetric operation," *Physical review letters*, vol. 116, no. 11, p. 110402, 2016.

[20] L. Hanschke, K. A. Fischer, S. Appel, D. Lukin, J. Wierzbowski, S. Sun, R. Trivedi, J. Vučković, J. J. Finley, and K. Müller, "Quantum dot single-photon sources with ultra-low multi-photon probability," *npj Quantum Information*, vol. 4, no. 1, p. 43, 2018.

[21] N. Akopian, N. Lindner, E. Poem, Y. Berlatzky, J. Avron, D. Gershoni, B. Gerardot, and P. Petroff, "Entangled photon pairs from semiconductor quantum dots," *Physical review letters*, vol. 96, no. 13, p. 130501, 2006.

[22] R. Stevenson, R. Thompson, A. Shields, I. Farrer, B. Kardynal, D. Ritchie, and M. Pepper, "Quantum dots as a photon source for passive quantum key encoding," *Physical Review B*, vol. 66, no. 8, p. 081302, 2002.

[23] H. Jayakumar, A. Predojević, T. Huber, T. Kauten, G. S. Solomon, and G. Weihs, "Deterministic photon pairs and coherent optical control of a single quantum dot," *Physical review letters*, vol. 110, no. 13, p. 135505, 2013.

[24] F. Wong, J. Shapiro, and T. Kim, "Efficient generation of polarization-entangled photons in a nonlinear crystal," *Laser physics*, vol. 16, no. 11, pp. 1517–1524, 2006.

[25] A. C. Dada, J. Leach, G. S. Buller, M. J. Padgett, and E. Andersson, "Experimental high-dimensional two-photon entanglement and violations of generalized Bell inequalities," *Nature Physics*, vol. 7, no. 9, p. 677, 2011.

[26] M. I. Dyakonov, "Basics of semiconductor and spin physics," in *Spin Physics in Semiconductors*, pp. 1–37, Springer, 2017.

[27] W. Metzger, M. Wanlass, L. Gedvilas, J. Verley, J. Carapella, and R. Ahrenkiel, "Effective electron mass and plasma filter characterization of n-type InGaAs and InAsP," *Journal of applied physics*, vol. 92, no. 7, pp. 3524–3529, 2002.

[28] T. Takagahara and K. Takeda, "Theory of the quantum confinement effect on excitons in quantum dots of indirect-gap materials," *Physical Review B*, vol. 46, no. 23, p. 15578, 1992.

[29] T. Takagahara, "Biexciton states in semiconductor quantum dots and their nonlinear optical properties," *Physical Review B*, vol. 39, no. 14, p. 10206, 1989.

[30] M. Bayer, G. Ortner, O. Stern, A. Kuther, A. Gorbunov, A. Forchel, P. Hawrylak, S. Fafard, K. Hinzer, T. Reinecke, *et al.*, "Fine structure of neutral and charged excitons in self-assembled In (Ga) As/(Al) GaAs quantum dots," *Physical Review B*, vol. 65, no. 19, p. 195315, 2002.

[31] M. Nirmal, D. J. Norris, M. Kuno, M. G. Bawendi, A. L. Efros, and M. Rosen, "Observation of the" dark exciton" in CdSe quantum dots," *Physical review letters*, vol. 75, no. 20, p. 3728, 1995.

[32] P. Michler, *Quantum dots for quantum information technologies*, vol. 237. Springer, 2017.

[33] G. Pettit and W. Turner, "Refractive index of InP," *Journal of Applied Physics*, vol. 36, no. 6, pp. 2081–2081, 1965.

[34] B. E. Saleh and M. C. Teich, *Fundamentals of photonics*. John Wiley & Sons, 2019.

[35] F. C. A. Pockels, *Lehrbuch der Kristalloptik*, vol. 19. BG Teubner, 1906.

[36] M. Parker, "The Kerr magneto-optic effect (1876–1976)," *Physica B+ C*, vol. 86, pp. 1171–1176, 1977.

[37] R. Weis and T. Gaylord, "Lithium niobate: summary of physical properties and crystal structure," *Applied Physics A*, vol. 37, no. 4, pp. 191–203, 1985.

[38] V. Palodiya and S. Raghuwanshi, "Performance Study of optical Modulator based on electrooptic effect," in *Journal of Physics: Conference Series*, vol. 735, p. 012071, IOP Publishing, 2016.

[39] T. Gorman and S. Haxha, "Full-Wave Comparison of Z-cut and X-cut Lithium Niobate (LiNbO3) Electrooptic Modulators Using Finite Element Method.," in *World Congress on Engineering*, pp. 459–464, 2007.

[40] J. W. Goodman, *Introduction to Fourier optics*. Roberts and Company Publishers, 2005.

[41] A. Papoulis, *Signal analysis*, vol. 191. McGraw-Hill New York, 1977.

[42] P. Horowitz and W. Hill, *The art of electronics*. Cambridge Univ. Press, 1989.

[43] F. Diedrich and H. Walther, "Nonclassical radiation of a single stored ion," *Physical review letters*, vol. 58, no. 3, p. 203, 1987.

[44] J. M. Martinis, S. Nam, J. Aumentado, and C. Urbina, "Rabi oscillations in a large Josephson-junction qubit," *Physical review letters*, vol. 89, no. 11, p. 117901, 2002.

[45] T. Stievater, X. Li, D. G. Steel, D. Gammon, D. Katzer, D. Park, C. Piermarocchi, and L. Sham, "Rabi oscillations of excitons in single quantum dots," *Physical Review Letters*, vol. 87, no. 13, p. 133603, 2001.

[46] G. Grynberg, A. Aspect, and C. Fabre, *Introduction to quantum optics: from the semi-classical approach to quantized light*. Cambridge university press, 2010.

[47] S. Stufler, P. Machnikowski, P. Ester, M. Bichler, V. Axt, T. Kuhn, and A. Zrenner, "Two-photon Rabi oscillations in a single In x Ga 1- x As/ Ga As quantum dot," *Physical Review B*, vol. 73, no. 12, p. 125304, 2006.

[48] M. Morinaga, "Deriving the static interaction between electric dipoles via the quantum gauge transformation," *arXiv preprint arXiv:1302.0920*, 2013.

[49] J. Villas-Bôas, S. E. Ulloa, and A. Govorov, "Decoherence of Rabi oscillations in a single quantum dot," *Physical review letters*, vol. 94, no. 5, p. 057404, 2005.

[50] A. Ramsay, T. Godden, S. Boyle, E. M. Gauger, A. Nazir, B. W. Lovett, A. Fox, and M. Skolnick, "Phonon-induced Rabi-frequency renormalization of optically driven single InGaAs/GaAs quantum dots," *Physical review letters*, vol. 105, no. 17, p. 177402, 2010.

[51] D. Mogilevtsev, A. Nisovtsev, S. Kilin, S. Cavalcanti, H. Brandi, and L. Oliveira, "Driving-dependent damping of Rabi oscillations in two-level semiconductor systems," *Physical review letters*, vol. 100, no. 1, p. 017401, 2008.

[52] A. J. Ramsay, A. V. Gopal, E. M. Gauger, A. Nazir, B. W. Lovett, A. M. Fox, and M. S. Skolnick, "Damping of Exciton Rabi Rotations by Acoustic Phonons in Optically Excited InGaAs/GaAs Quantum Dots," *Phys. Rev. Lett.*, vol. 104, p. 017402, Jan 2010.

[53] P. Machnikowski and L. Jacak, "Resonant nature of phonon-induced damping of Rabi oscillations in quantum dots," *Phys. Rev. B*, vol. 69, p. 193302, May 2004.

[54] A. Nazir, "Photon statistics from a resonantly driven quantum dot," *Phys. Rev. B*, vol. 78, p. 153309, Oct 2008.

[55] D. P. McCutcheon and A. Nazir, "Quantum dot Rabi rotations beyond the weak exciton–phonon coupling regime," *New Journal of Physics*, vol. 12, no. 11, p. 113042, 2010.

[56] C. Roy and S. Hughes, "Phonon-Dressed Mollow Triplet in the Regime of Cavity Quantum Electrodynamics: Excitation-Induced Dephasing and Nonperturbative Cavity Feeding Effects," *Phys. Rev. Lett.*, vol. 106, p. 247403, Jun 2011.

[57] I. Wilson-Rae and A. Imamoğlu, "Quantum dot cavity-QED in the presence of strong electron-phonon interactions," *Phys. Rev. B*, vol. 65, p. 235311, May 2002.

[58] D. P. McCutcheon, N. S. Dattani, E. M. Gauger, B. W. Lovett, and A. Nazir, "A general approach to quantum dynamics using a variational master equation: Application to phonon-damped Rabi rotations in quantum dots," *Physical Review B*, vol. 84, no. 8, p. 081305, 2011.

[59] G. Bacher, R. Weigand, J. Seufert, V. Kulakovskii, N. Gippius, A. Forchel, K. Leonardi, and D. Hommel, "Biexciton versus exciton lifetime in a single semiconductor quantum dot," *Physical Review Letters*, vol. 83, no. 21, p. 4417, 1999.

[60] B. R. Fisher, H.-J. Eisler, N. E. Stott, and M. G. Bawendi, "Emission intensity dependence and single-exponential behavior in single colloidal quantum dot fluorescence lifetimes," *The Journal of Physical Chemistry B*, vol. 108, no. 1, pp. 143–148, 2004.

[61] D. P. DiVincenzo, "The physical implementation of quantum computation," *Fortschritte der Physik: Progress of Physics*, vol. 48, no. 9-11, pp. 771–783, 2000.

[62] M. Prilmüller, T. Huber, M. Müller, P. Michler, G. Weihs, and A. Predojević, "Hyperentanglement of photons emitted by a quantum dot," *Physical review letters*, vol. 121, no. 11, p. 110503, 2018.

[63] M. Gimeno-Segovia, T. Rudolph, and S. E. Economou, "Deterministic generation of large-scale entangled photonic cluster state from interacting solid state emitters," *Physical review letters*, vol. 123, no. 7, p. 070501, 2019.

[64] D. Press, K. De Greve, P. L. McMahon, T. D. Ladd, B. Friess, C. Schneider, M. Kamp, S. Höfling, A. Forchel, and Y. Yamamoto, "Ultrafast optical spin echo in a single quantum dot," *Nature Photonics*, vol. 4, no. 6, p. 367, 2010.

[65] S. Yamada and M. Minakata, "DC drift phenomena in LiNbO3 optical waveguide devices," *Japanese Journal of Applied Physics*, vol. 20, no. 4, p. 733, 1981.

[66] D. Dalacu, "`https://science.uottawa.ca/physics/people/dalacu-dan`." University of Ottawa,Canada.

[67] D. Dalacu, A. Kam, D. G. Austing, X. Wu, J. Lapointe, G. C. Aers, and P. J. Poole, "Selective-area vapour–liquid–solid growth of InP nanowires," *Nanotechnology*, vol. 20, no. 39, p. 395602, 2009.

[68] D. Dalacu, K. Mnaymneh, J. Lapointe, X. Wu, P. J. Poole, G. Bulgarini, V. Zwiller, and M. E. Reimer, "Ultraclean emission from InAsP quantum dots in defect-free wurtzite InP nanowires," *Nano letters*, vol. 12, no. 11, pp. 5919–5923, 2012.

[69] R. W. Boyd, *Nonlinear optics*. Elsevier, 2003.

[70] M. Khoshnegar, T. Huber, A. Predojević, D. Dalacu, M. Prilmüller, J. Lapointe, X. Wu, P. Tamarat, B. Lounis, P. Poole, *et al.*, "A solid state source of photon triplets based on quantum dot molecules," *Nature communications*, vol. 8, p. 15716, 2017.

[71] N. H. Lindner and T. Rudolph, "Proposal for pulsed on-demand sources of photonic cluster state strings," *Physical review letters*, vol. 103, no. 11, p. 113602, 2009.

[72] I. Schwartz, D. Cogan, E. R. Schmidgall, Y. Don, L. Gantz, O. Kenneth, N. H. Lindner, and D. Gershoni, "Deterministic generation of a cluster state of entangled photons," *Science*, vol. 354, no. 6311, pp. 434–437, 2016.

[73] H. De Riedmatten, I. Marcikic, H. Zbinden, and N. Gisin, "Creating high dimensional time-bin entanglement using mode-locked lasers," *arXiv preprint quant-ph/0204165*, 2002.

[74] F. Vedovato, C. Agnesi, M. Tomasin, M. Avesani, J.-Å. Larsson, G. Vallone, and P. Villoresi, "Postselection-loophole-free Bell violation with genuine time-bin entanglement," *Physical review letters*, vol. 121, no. 19, p. 190401, 2018.

[75] D. J. Griffiths and D. F. Schroeter, *Introduction to quantum mechanics*. Cambridge University Press, 2018.

[76] "The NIST Reference on constants, Units, and Uncertainty." `https://physics.nist.gov/cuu/Constants/index.html`. Accessed: 2019-09-23.

5 Acknowledgements

I would like to use this opportunity to express my gratitude to the people that supported me throughout my studies. First I want to thank my mother Sigrid and my brother Fabian for always being a supportive family and providing a feeling of "home" during my stays in Graz. I also want to thank my father Frank and his wife Claudia for sparking my interest in physics at a young age and encouraging my decision to spent a year abroad during my studies.
Special thanks to my girlfriend Miriam and her daughter Mia for always being my warm fire during those lonely and dark days you sometimes experience when you move to a new place. Also this thesis would have looked a lot more like a twelve-year-old's work if it weren't for her ability to sniff out (almost) every grammar and spelling error I made.
Finally I want to thank Max Prillmüller for teaching me how to properly work in a laser lab without risking an eye and Professor Gregor Weihs for giving me the opportunity to join his group and being very supportive with every question I had.

A Appendix

A.1 Three dimensional infinite well

In this section the eigenfunctions and eigenenergies of a three dimensional infinite well are calculated. The potential of such a problem is written as

$$V(x,y,z) = \begin{cases} 0 \text{ if } 0<x<L_x \wedge 0<y<L_y \wedge 0<z<L_z \\ \infty \text{ else} \end{cases} \tag{A.1}$$

which describes a box of size $L_x \times L_y \times L_z$. Assuming that each direction can be described independent of the other two the ansatz for the wavefunction is chosen as

$$\psi(\mathbf{r}) = \psi_x(x)\psi_y(y)\psi_z(z) \tag{A.2}$$

with

$$\psi_l(l) = A_l e^{ik_l l} + B_l e^{-ik_l l} \tag{A.3}$$

where $l \in \{x,y,z\}$. This results in three identical one dimensional problems that can be solved independent of each other. By invoking the first boundary condition that the wavefunction can not exist outside the well ($l \leq 0$)

$$\psi_l(l=0) = 0 = A_l + B_l \tag{A.4}$$

the constant B_l is determined to be $-A_l$ which lets equation (A.3) become

$$\psi_l(l) = Ae^{ik_l l} - Ae^{-ik_l l} = \overbrace{i2A}^{\tilde{A}} \sin(k_l l). \tag{A.5}$$

Here the identity $\sin(x) = \frac{1}{i2}(e^{ix} - e^{-ix})$ is used and a new constant $\tilde{A}$ is introduced. Invoking the second boundary condition that for $l \geq L_l$ the wavefunction also has to vanish gives

$$\psi_l(l=L_l) = 0 = \tilde{A}\sin(k_l L_l). \tag{A.6}$$

This condition is fulfilled if $k_l L_l = n\pi$ with $n \in \mathbb{N}_{\neq 0}$. An expression for

$$k_l = \frac{n\pi}{L_l} \tag{A.7}$$

is found. Finally, by utilising the regular normalisation condition

$$\int_0^{L_l} \|\psi_l(l)\|^2 dl = 1 = \int_0^{L_l} \tilde{A}^2 \sin^2(\frac{n\pi}{L_l} l) dl \tag{A.8}$$

$\tilde{A}$ is found to has a value of $\sqrt{\frac{2}{L_l}}$. The final form of the one dimensional wavefunction equation (A.3) is

$$\psi_l^n(l) = \sqrt{\frac{2}{L_l}} \sin\left(\frac{n\pi}{L_l} l\right). \tag{A.9}$$

Solving the time-independent one dimensional Schrödinger equation

$$\frac{-\hbar^2}{2m} \frac{\partial^2}{\partial l^2} \psi_l^n(l) + V(l)\psi_l^n(l) = E_n \psi_l^n(l) \tag{A.10}$$

for eigenenergies E_n yields

$$E_n = \frac{\hbar^2 \pi^2 n^2}{2mL_l^2}. \tag{A.11}$$

The solutions to the one dimensional infinite well equation (A.9) and equation (A.11) are illustrated in figure 32 and a detailed treatment can also be found in various introductory textbooks, e.g. [75].

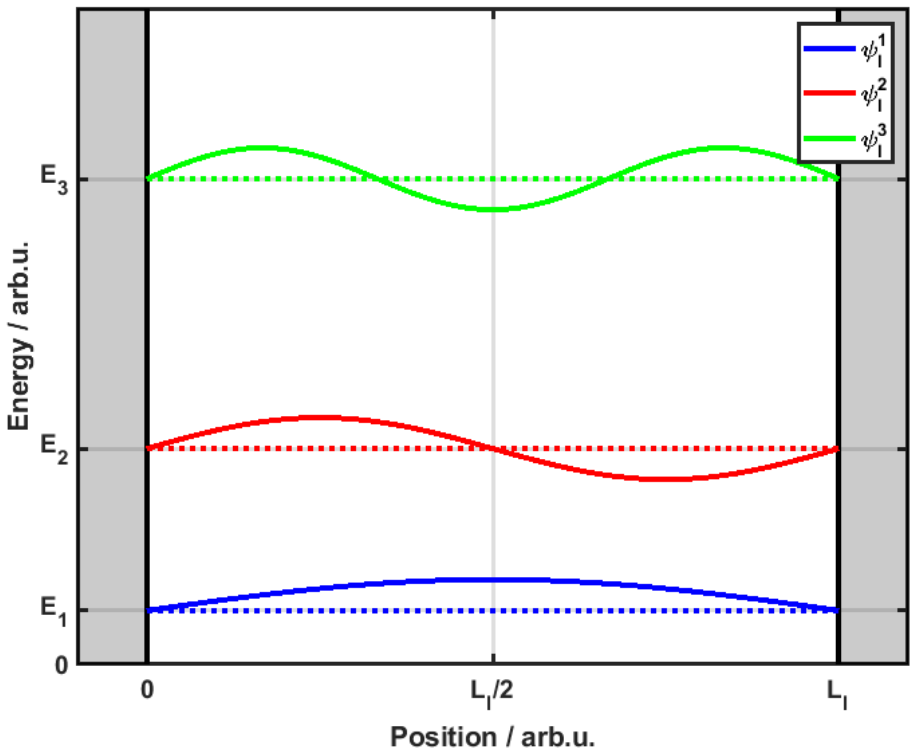

Figure 32: Solutions to the one dimensional infinite well problem for eigenenergies E_n with $n \in \{1, 2, 3\}$. If n is an odd number the corresponding wavefunction ψ_l^n is symmetric around $L_l/2$, while for an even quantum number n the solution is antisymmetric.

Generalizing the solution for three dimensions via equation (A.2) gives an expression for the eigenenergies

$$E_{n_x,n_y,n_z} = \frac{\hbar^2\pi^2}{2m}(\frac{n_x^2}{L_x^2} + \frac{n_y^2}{L_y^2} + \frac{n_z^2}{L_z^2}) \tag{A.12}$$

depending on the quantum numbers $n_x, n_y, n_z \in \mathbb{N}_{\neq 0}$. This expression is further discussed in section 2.1.2.

A.2 Derivation of the atomic Hamiltonian

A justification of the Hamiltonian 2.21 in section 2.4 is presented here by relating the quantum mechanical motion of a charged particle under the influence of an electromagnetic field to its classical counterpart. This derivation follows [46]. The classical equation of motion for charged particles is called the Newton-Lorentz equation and reads as follows:

$$m\frac{d\mathbf{v}}{dt} = q(\mathbf{v} \times \mathbf{B}(\mathbf{r}(t), t) + \mathbf{E}(\mathbf{r}(t), t)) \tag{A.13}$$

where $\mathbf{v}$ is the velocity of a particle with charge q and $\mathbf{E}(\mathbf{r}(t), t)$ and $\mathbf{B}(\mathbf{r}(t), t))$ are the electric and magnetic fields acting on it. $\mathbf{E}(\mathbf{r}, t)$ and $\mathbf{B}(\mathbf{r}, t)$ are related to the potentials $\mathbf{A}(\mathbf{r}, t)$ and $U(\mathbf{r}, t)$ via:

$$\mathbf{E}(\mathbf{r}, t) = -\frac{\partial \mathbf{A}(\mathbf{r}, t)}{\partial t} - \boldsymbol{\nabla} U(\mathbf{r}, t) \tag{A.14}$$

$$\mathbf{B}(\mathbf{r}, t)) = \boldsymbol{\nabla} \times \mathbf{A}(\mathbf{r}, t) \tag{A.15}$$

Showing that equation (2.21) results in a quantum mechanical expression that is in agreement with the experimentally verified classical equation of motion (equation (A.13)) justifies this Hamiltonian to describe the system.

Quantum mechanical equations of motion

First, the velocity operator $\hat{\mathbf{v}}$ has to be introduced such that

$$\langle \hat{\mathbf{v}} \rangle = \frac{\mathrm{d}}{\mathrm{d}t} \langle \hat{\mathbf{r}} \rangle , \tag{A.16}$$

with $\langle \hat{a} \rangle$ being the expectation value of an operator $\hat{a}$. The time derivative of an operator is defined as:

$$\frac{\mathrm{d}}{\mathrm{d}t} \langle \hat{a} \rangle = \frac{1}{i\hbar} \left\langle \left[\hat{a}, \hat{H}\right] \right\rangle + \left\langle \frac{\partial \hat{a}}{\partial t} \right\rangle \tag{A.17}$$

with $\left[\hat{a}, \hat{H}\right] = \hat{a}\hat{H} - \hat{H}\hat{a}$ being the commutator of $\hat{a}$ and $\hat{H}$. This equation can be used to describe the right hand side of equation (A.16). $U(\hat{\mathbf{r}}, t)$ only contains the position

operator $\hat{\mathbf{r}} = (\hat{x}, \hat{y}, \hat{z})^T$ and therefore commutes with any element of $\hat{\mathbf{r}}$. As a result the commutator of equation (A.17) can be written as

$$\left\langle \left[\hat{u}, \hat{H}\right] \right\rangle = i\hbar \left\langle \frac{\hat{p}_u - qA_u(\hat{\mathbf{r}}, t)}{m} \right\rangle \tag{A.18}$$

where $u \in \{x, y, z\}$. Since the position operator does not explicitly depend on time explicitly the second term on the right hand side of equation (A.17) is zero and equation (A.17) can be written as

$$\frac{\mathrm{d}\left\langle \hat{u} \right\rangle}{\mathrm{d}t} = \left\langle \frac{\hat{p}_u - qA_u(\hat{\mathbf{r}}, t)}{m} \right\rangle. \tag{A.19}$$

This leads to an expression for the velocity operator $\hat{\mathbf{v}}$ of

$$\hat{\mathbf{v}} = \frac{\hat{\mathbf{p}} - q\mathbf{A}(\hat{\mathbf{r}}, t)}{m}. \tag{A.20}$$

The derivative of the left hand side of equation (A.13) can again be evaluated using equation (A.17)

$$\frac{\mathrm{d}\left\langle \hat{v}_u \right\rangle}{\mathrm{d}t} = \frac{1}{i\hbar} \left\langle \left[\hat{v}_u, \hat{H}\right] \right\rangle + \left\langle \frac{\partial \hat{v}_u}{\partial t} \right\rangle. \tag{A.21}$$

This time the second term on the right hand side depends explicitly on time since $\mathbf{A}(\hat{\mathbf{r}}, t)$ shows time dependence and using equation (A.20) it reads as

$$\frac{\partial \hat{v}_u}{\partial t} = -\frac{q}{m} \frac{\partial A_u(\hat{\mathbf{r}}, t)}{\partial t}. \tag{A.22}$$

In order to evaluate the commutator of equation (A.21) it is helpful to rewrite equation (2.21) in terms of $\hat{\mathbf{v}}$

$$\hat{H} = \frac{m\hat{\mathbf{v}}^2}{2} + qU(\hat{\mathbf{r}}, t). \tag{A.23}$$

Utilising the properties of the commutator operation $\left[\hat{A} + \hat{B}, \hat{C}\right] = \left[\hat{A}, \hat{C}\right] + \left[\hat{B}, \hat{C}\right]$, $\left[\hat{A}, \hat{A}\right] = 0$ and $\left[\hat{A}, \hat{B}\hat{C}\right] = \left[\hat{A}, \hat{B}\right]\hat{C} + \hat{B}\left[\hat{A}, \hat{C}\right]$ the commutator of equation (A.21) reads as

$$\left[\hat{v}_x, \hat{H}\right] = \frac{m}{2}(\left[\hat{v}_x, \hat{v}_y^2\right] + \left[\hat{v}_x, \hat{v}_z^2\right]) + q[\hat{v}_x, U(\hat{\mathbf{r}}, t)] \tag{A.24}$$

with $u = x$ for a better geometrical understanding and

$$\left[\hat{v}_x, \hat{v}_y^2\right] = \hat{v}_y[\hat{v}_x, \hat{v}_y] + [\hat{v}_x, \hat{v}_y]\hat{v}_y. \tag{A.25}$$

Investigating the first commutator on the right hand side of equation (A.25) and using equation (A.20) leads to the expression

$$[\hat{v}_x, \hat{v}_y] = -\frac{q}{m^2}([\hat{p}_x, A_y(\hat{\mathbf{r}}, t)] + [A_x(\hat{\mathbf{r}}, t), \hat{p}_y] \tag{A.26}$$

which, by applying the generalised form of the canonical commutation relation $[\hat{p}_u, g(\hat{\mathbf{r}})] = -i\hbar\frac{\partial g(\hat{\mathbf{r}})}{\partial u}$ and equation (A.15), can be evaluated to be equal to

$$[\hat{v}_x, \hat{v}_y] = \frac{i\hbar q}{m^2}(\frac{\partial A_y(\hat{\mathbf{r}}, t)}{\partial x} - \frac{\partial A_x(\hat{\mathbf{r}}, t)}{\partial y}) = \frac{i\hbar q}{m^2}B_z(\hat{\mathbf{r}}, t). \tag{A.27}$$

Substituting into equation (A.25) yields

$$\left[\hat{v}_x, \hat{v}_y^2\right] = \frac{i\hbar q}{m^2}(\hat{v}_y B_z(\hat{\mathbf{r}}, t) + B_z(\hat{\mathbf{r}}, t)\hat{v}_y) \tag{A.28}$$

and similarly for the second commutator of equation (A.24)

$$\left[\hat{v}_x, \hat{v}_z^2\right] = \frac{i\hbar q}{m^2}(\hat{v}_z B_y(\hat{\mathbf{r}}, t) + B_y(\hat{\mathbf{r}}, t)\hat{v}_z). \tag{A.29}$$

The final commutator of equation (A.24) can be simplified by again using the generalised form of the canonical commutation relation and gives

$$[\hat{v}_x, U(\hat{\mathbf{r}}, t)] = \frac{1}{m}[\hat{p}_x, U(\hat{\mathbf{r}}, t)] = -\frac{i\hbar}{m}\frac{\partial U(\hat{\mathbf{r}}, t)}{\partial x}. \tag{A.30}$$

Substituting equation (A.22) and equation (A.30) into equation (A.21) finally gives the result

$$\frac{\mathrm{d}\left\langle \hat{v}_x \right\rangle}{\mathrm{d}t} = \frac{q}{m}(\frac{1}{2}\left\langle \hat{v}_y\hat{B}_z - \hat{v}_z\hat{B}_y + \hat{B}_z\hat{v}_y - \hat{B}_y\hat{v}_z \right\rangle - \left\langle \frac{\partial U(\hat{\mathbf{r}}, t)}{\partial x} + \frac{\partial A_x(\hat{\mathbf{r}}, t)}{\partial t} \right\rangle). \tag{A.31}$$

Evaluating $\frac{\mathrm{d}\langle \hat{v}_y \rangle}{\mathrm{d}t}$ and $\frac{\mathrm{d}\langle \hat{v}_z \rangle}{\mathrm{d}t}$ in a similar fashion, relating the right hand side of equation (A.31) to the electric field via equation (A.14) and the cross product $\mathbf{v} \times \mathbf{B}$ gives the vector equation

$$m\frac{\mathrm{d}\left\langle \hat{\mathbf{v}} \right\rangle}{\mathrm{d}t} = q\left\langle \frac{\hat{\mathbf{v}} \times \mathbf{B}(\hat{\mathbf{r}}, t) - \mathbf{B}(\hat{\mathbf{r}}, t) \times \hat{\mathbf{v}}}{2} \right\rangle + q\left\langle \mathbf{E}(\hat{\mathbf{r}}, t) \right\rangle \tag{A.32}$$

which looks very similar to equation (A.13). Equation (A.32) is the quantum mechanical analogue of the classical equation of motion for a charged particle in an electromagnetic field. Showing that the Hamiltonian of equation (2.21) results in motion that is in agreement with the well understood classical theory, indicates that the Hamiltonian indeed describes the motion of charged particles and can be used to describe the interaction of an electron bound to a nucleus under the influence of an electromagnetic field.

A.3 Solving for Rabi oscillations

In this section the transition probability equation (2.46) is calculated starting from the Hamiltonian shown in equation (2.45). Since the Hamiltonian consists of two separate terms $\hat{H} = \hat{H}_0 + \hat{H}_1$ where $\hat{H}_0$ is the regular atomic Hamiltonian, a wave-function of the form

$$|\Psi\rangle = \alpha_0(t)e^{-\frac{i}{\hbar}\hat{H}_0 t}|0\rangle + \alpha_1(t)e^{-\frac{i}{\hbar}\hat{H}_0 t}|1\rangle \tag{A.33}$$

is a suitable ansatz. $|0\rangle$ and $|1\rangle$ are eigenstates of $\hat{H}_0$ and $\alpha_0(t)$ and $\alpha_1(t)$ are time dependent variables for which the usual normalisation condition

$$\|\alpha_0(t)\|^2 + \|\alpha_1(t)\|^2 = 1 \tag{A.34}$$

must be fulfilled. Since $|0\rangle$ and $|1\rangle$ are eigenstates of $\hat{H}_0$, the time evolution can be transformed via $e^{-\frac{i}{\hbar}\hat{H}t}|n\rangle = e^{-\frac{i}{\hbar}E_n t}|n\rangle$ where $|n\rangle$ are eigenstates of $\hat{H}$ with corresponding eigenenergies E_n. As stated by equation (2.41) the eigenenergies of $|0\rangle$ and $|1\rangle$ are $-\frac{\omega_0}{2}$ and $+\frac{\omega_0}{2}$ respectively and ω_0 represents the atomic transition frequency. This lets $|\Psi\rangle$ become

$$|\Psi\rangle = \alpha_0(t)e^{\frac{i}{\hbar}\frac{\omega_0}{2}t}|0\rangle + \alpha_1(t)e^{-\frac{i}{\hbar}\frac{\omega_0}{2}t}|1\rangle\,. \tag{A.35}$$

Pulling out and dropping a common phase $e^{\frac{i}{\hbar}\frac{\omega_0}{2}t}$ leaves

$$|\Psi\rangle = \alpha_0(t)|0\rangle + e^{-\frac{i}{\hbar}\omega_0 t}|1\rangle \tag{A.36}$$

which is the same as shifting the zero-energy point such that $E_0 = 0$. This lets the Hamiltonian of equation (2.45) be written as:

$$\hat{H} = \hbar\begin{pmatrix} 0 & \Omega_0\cos(\omega t) \\ \Omega_0\cos(\omega t) & \omega_0 \end{pmatrix} = \hbar(\Omega_0\cos(\omega t)(|0\rangle\langle 1| + |1\rangle\langle 0|) + \omega_0|1\rangle\langle 1|) \tag{A.37}$$

where Ω_0 describes the coupling strength in the dipole approximation (equation (2.44)).

Time evolution of quantum systems is governed by Schrödinger's equation

$$i\hbar\frac{\mathrm{d}}{\mathrm{d}t}|\Psi\rangle = \hat{H}|\Psi\rangle \tag{A.38}$$

and projecting onto the eigenstate $\langle 0|$ gives

$$i\hbar\langle 0|\frac{\mathrm{d}}{\mathrm{d}t}|\Psi\rangle = \langle 0|\hat{H}|\Psi\rangle \tag{A.39}$$

$$i\dot{\alpha_0} = \Omega_0\cos(\omega t)\alpha_1 e^{-i\omega_0 t} \tag{A.40}$$

with $\dot{\alpha_i} = \frac{\mathrm{d}}{\mathrm{d}t}\alpha_i(t)$. Using the identity $\cos(x) = \frac{1}{2}(e^{ix} + e^{-ix})$ equation (A.40) can be rewritten as

$$i\dot{\alpha_0} = \frac{\Omega_0 \alpha_1}{2}(e^{-i(\omega_0-\omega)t} + e^{-i(\omega_0+\omega)t}). \tag{A.41}$$

Calling $\Delta = \omega_0 - \omega$ the detuning and applying the rotating wave approximation assuming $\Delta \ll \omega_0 + \omega$ gives the first order differential equation

$$i\dot{\alpha_0} = \frac{\Omega_0 \alpha_1}{2} e^{-i\Delta t}. \tag{A.42}$$

Following the same steps for projecting onto the eigenstate $\langle 1|$ results in another first order differential equation

$$i\dot{\alpha_1} = \frac{\Omega_0 \alpha_0}{2} e^{i\Delta t} \tag{A.43}$$

which is coupled to equation (A.42) via α_0. Decoupling these equations is achieved by performing another time derivative on equation (A.43)

$$i\ddot{\alpha_1} = \frac{\Omega_0}{2}\dot{\alpha_0} e^{i\Delta t} + i\Delta \frac{\Omega_0}{2} \alpha_0 e^{i\Delta t}. \tag{A.44}$$

Substituting equation (A.42) and equation (A.43) into equation (A.44) yields the uncoupled second order differential equation

$$0 = \ddot{\alpha_1} - i\Delta\dot{\alpha_1} + \frac{\Omega_0^2}{4}\alpha_1. \tag{A.45}$$

Using the ansatz $\alpha_1(t) = e^{i\lambda t}$ and evaluating equation (A.45) gives

$$0 = \lambda^2 - \Delta\lambda - \frac{\Omega_0^2}{4} \tag{A.46}$$

which has two solutions for λ, namely

$$\lambda_{1,2} = \frac{\Delta \pm \sqrt{\Delta^2 + \Omega^2}}{2}. \tag{A.47}$$

The general solution to this problem is given by

$$\alpha_1 = A \exp\left(i\frac{\Delta + \sqrt{\Delta^2 + \Omega_0^2}}{2}t\right) + B \exp\left(i\frac{\Delta - \sqrt{\Delta^2 + \Omega_0^2}}{2}t\right). \tag{A.48}$$

If the system at $t = 0$ is known to be in state $|0\rangle$ the starting condition $\|\alpha_1(t=0)\|^2 = 0$ defines A and B to have the relation $A = -B$ and rewriting $\Omega = \sqrt{\Delta^2 + \Omega_0^2}$ gives

$$\alpha_1 = Ae^{i\frac{\Delta}{2}t}(e^{i\frac{\Omega}{2}t} - e^{-i\frac{\Omega}{2}t}). \tag{A.49}$$

Using another identity $\sin(x) = \frac{1}{i2}(e^{ix} - e^{-ix})$ leads to the expression

$$\alpha_1 = Ai2e^{i\frac{\Delta}{2}t} \sin\left(\frac{\Omega}{2}t\right). \tag{A.50}$$

Together with equation (A.43) this gives an expression for α_0

$$\alpha_0 = i\frac{2}{\Omega_0}e^{-i\Delta t}\dot{\alpha_1} = -A\frac{2}{\Omega_0}e^{-i\frac{\Delta}{2}t}(i\Delta\sin\left(\frac{\Omega}{2}t\right) + \cos\left(\frac{\Omega}{2}t\right)\Omega) \tag{A.51}$$

and by invoking the second starting condition $\|\alpha_0(t=0)\|^2 = 1$, A is determined by

$$A = -\frac{\Omega_0}{2\Omega}. \tag{A.52}$$

Finally α_1 can be written as

$$\alpha_1 = -i\frac{\Omega_0}{\Omega}e^{i\frac{\Delta}{2}t}\sin\left(\frac{\Omega}{2}t\right) \tag{A.53}$$

and since $\|\alpha_1(t)\|^2$ is an expression for the probability of finding the system in state $|1\rangle$ at a given time t the final result is

$$P_{0\to1}(t) = \|\alpha_1(t)\|^2 = \frac{\Omega_0^2}{\Omega^2}\sin^2(\frac{\Omega}{2}t). \tag{A.54}$$

Equation (2.46) is thereby calculated by evaluating the time evolution of the Hamiltonian equation (A.37) and further discussed in section 2.4.

A.4 Life times of two coupled energy levels

In this section the model used in section 2.5 to describe the radiative behaviour of two coupled energy levels is derived. The coupled rate equations of equation (2.48) can be written in matrix representation as

$$\begin{pmatrix}\dot{N}_{XX}\\ \dot{N}_X\end{pmatrix} = \begin{pmatrix}-\Gamma_{XX} & 0\\ \Gamma_{XX} & -\Gamma_X\end{pmatrix}\begin{pmatrix}N_{XX}\\ N_X\end{pmatrix} \tag{A.55}$$

where $\dot{N}_{XX} = \frac{\mathrm{d}N_{XX}}{\mathrm{d}t}$ and $\dot{N}_X = \frac{\mathrm{d}N_X}{\mathrm{d}t}$. Solving the eigenvalue and eigenvector problem of the coefficient matrix gives the eigenvalues λ_i and the corresponding eigenvectors $\mathbf{v}_i$.

$$\begin{aligned}\lambda_1 &= -\Gamma_{XX} \quad ;\ \mathbf{v}_1 = \begin{pmatrix}1\\ -\frac{\Gamma_{XX}}{\Gamma_{XX}-\Gamma_X}\end{pmatrix}\\ \lambda_2 &= -\Gamma_X \quad ;\ \mathbf{v}_2 = \begin{pmatrix}0\\ 1\end{pmatrix}\end{aligned} \tag{A.56}$$

This lets the general solution be constructed as:

$$\begin{pmatrix}N_{XX}\\ N_X\end{pmatrix} = A\mathbf{v}_1e^{\lambda_1t} + B\mathbf{v}_2e^{\lambda_2t} = A\begin{pmatrix}1\\ -\frac{\Gamma_{XX}}{\Gamma_{XX}-\Gamma_X}\end{pmatrix}e^{-\Gamma_{XX}t} + B\begin{pmatrix}0\\ 1\end{pmatrix}e^{-\Gamma_Xt}. \tag{A.57}$$

Using the starting condition $N_{XX}(t = 0) = N_0$, meaning that the occupation of the $|XX\rangle$ state at $t = 0$ is known, determines the constant $A = N_0$. Assuming that all particles start off in the $|XX\rangle$ state gives the second starting condition $N_X(t = 0) = 0$ and specifies the constant B via

$$N_X(t = 0) = 0 = -N_0 \frac{\Gamma_{XX}}{\Gamma_{XX} - \Gamma_X} + B \Rightarrow B = N_0 \frac{\Gamma_{XX}}{\Gamma_{XX} - \Gamma_X}. \tag{A.58}$$

This leads to the final expression of

$$\begin{aligned} N_{XX} &= N_0 e^{-\Gamma_{XX} t} \\ N_X &= N_0 \frac{\Gamma_{XX}}{\Gamma_{XX} - \Gamma_X} (e^{-\Gamma_X t} - e^{-\Gamma_{XX} t}) \end{aligned} \tag{A.59}$$

which is used to model the time dependent radiative behaviour of the biexciton state feeding into the exciton state and utilised in section 3.2.2 to extract lifetime values.

A.5 Natural constants

Table 5: List of constants of nature used in this work. If no uncertainty is shown the value is expected to be known exactly. Values and uncertainties are taken from [76].

Symbol	Name of constant	Value and standard uncertainty
$\hbar$	reduced Planck constant	$1.054\,571\,817 \times 10^{-34}\,\mathrm{J\,s}$
m_e	electron mass	$9.109\,383\,701\,5(28) \times 10^{-31}\,\mathrm{kg}$
k_B	Boltzmann constant	$1.380\,649 \times 10^{-23}\,\mathrm{J\,K^{-1}}$
ϵ_0	vacuum electric permittivity	$8.854\,187\,812\,8(13) \times 10^{-12}\,\mathrm{F\,m^{-1}}$

A.6 Additional information

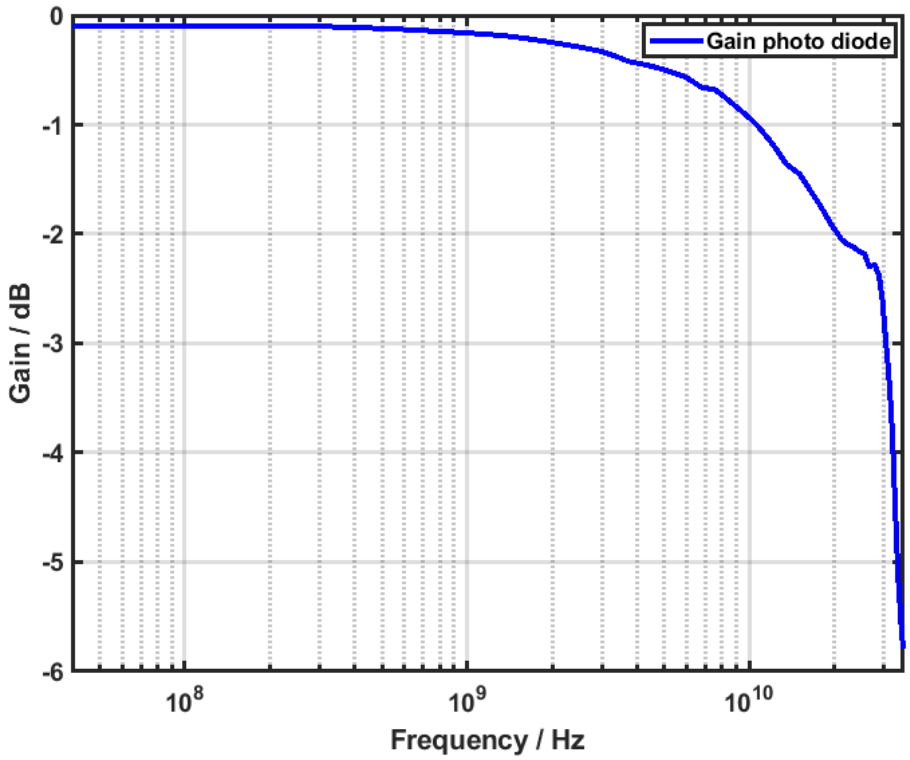

Figure 33: Bode diagram of the photo-diode (D_{RF}, DXM30AF) provided by the manufacturing company (Thorlabs).